VU Research Portal

Scattering matrices of mineral particles at 441.6 nm and 632.8 nm.

Volten, H.; Munoz, O.; Rol, E.; de Haan, J.F.; Vassen, W.; Hovenier, J.W.; Muinonen, K.; Nousiainen, T.

Link to publication in VU Research Portal

Scattering matrices of mineral aerosol particles at 441.6 nm and 632.8 nm

H. Volten, O. Muñoz,[1] E. Rol,[2] J.F. de Haan, W. Vassen, and J.W. Hovenier[2]

Department of Physics and Astronomy, Free University, Amsterdam, Netherlands

K. Muinonen

Observatory, University of Helsinki, Finland

T. Nousiainen

Department of Meteorology, University of Helsinki, Finland

Abstract. We present measured scattering matrices as functions of the scattering angle in the range 5°-173° and at wavelengths of 441.6 nm and 632.8 nm for seven distinct irregularly shaped mineral aerosol samples with properties representative of mineral aerosols present in the Earth's atmosphere. The aerosol samples, i.e., feldspar, red clay, quartz, loess, Pinatubo and Lokon volcanic ash, and Sahara sand, represent a wide variety of particle size (typical diameters between 0.1 and 100 μm) and composition (mainly silicates). We investigate the effects of differences in size and complex refractive index on the light-scattering properties of these irregular particles. In particular, we find that the measured scattering matrix elements when plotted as functions of the scattering angle are confined to rather limited domains. This similarity in scattering behavior justifies the construction of an average aerosol scattering matrix as a function of scattering angle to facilitate, for example, the use of our results for the interpretation of remote sensing data. We show that results of ray-optics calculations, using Gaussian random shapes, are able to describe the experimental data well when taking into account the high irregularity in shape of the aerosols, even when these aerosols are rather small. Using the results of ray-optics calculations, we interpret the differences found between the measured aerosol scattering matrices in terms of differences in complex refractive index and particle size relative to the wavelength. The importance of our results for studies of astronomical objects, such as planets, comets, asteroids, and circumstellar dust shells is discussed.

1. Introduction

A large mass fraction of the aerosols in the Earth's atmosphere consists of irregular mineral particles. These aerosols affect climate directly by interacting with solar and terrestrial radiation and indirectly by their effects on cloud microphysics as well as on cloud albedo. For instance, the presence of desert aerosol particles causes significant changes in the air temperature over

---

[1] Also at Instituto de Astrofísica de Andalucía (CSIC), Granada, Spain.

[2] Also at Astronomical Institute 'Anton Pannekoek,' University of Amsterdam, Amsterdam, Netherlands.

the world's main deserts and oceans [e.g., *Gerber and Deepak*, 1984; *Nakajima et al.*, 1989; *Husar et al.*, 1997; *Miller and Tegen*, 1998].

Desert regions, such as the Sahara, are the main source for mineral aerosols on Earth [*d'Almeida et al.*, 1991]. Volcanic eruptions are another important source of such aerosols. The global source strength of mineral aerosols is currently estimated to be $1 - 5 \times 10^{12}$ kg/yr [*Tegen and Fung*, 1995]. However, the production rate of such aerosols is highly variable in space and time since it depends on the prevailing atmospheric conditions, on the type of surface underneath the atmosphere, and on the strength and frequency of volcanic eruptions. Mineral aerosols can be found in the Earth's atmosphere being blown away from their origin up to thousands of kilometers [*Schütz*, 1980; *Prospero et al.*, 1981; *Rietmeijer*, 1993]. The mean diameters of mineral aerosols vary roughly between 0.02 μm and 100 μm [*d'Almeida*

et al., 1991]. Most of these particles are irregularly shaped [e.g., *Okada et al.*, 1987].

Research on the properties of terrestrial mineral aerosol particles is not only important for studies of the Earth's atmosphere but also for astronomical research. Recent investigations indicate that properties of terrestrial mineral particles are similar to the mineral particles found on other planets and solar system bodies, such as asteroids and comets, as well as to interplanetary, circumstellar and interstellar particles [e.g., *Weiss-Wrana*, 1983; *Jäger et al.*, 1994; *Moroz et al.*, 1994; *Pollack et al.*, 1994; *Colangeli et al.*, 1995; *Molster et al.*, 1999]. In many of these astronomical investigations, (polarized) scattered light is an important source of information [e.g., *Hansen and Hovenier*, 1974; *Chernova et al.*, 1993; *Levasseur-Regourd et al.*, 1996], because it is difficult to collect extraterrestrial particles or to investigate them in situ.

Scattering matrices as functions of the scattering angle of irregular mineral aerosol particles play an important role in radiative transfer processes. First, scattering matrices contain all polarizing properties of the scatterers and are, for example, indispensable for accurate calculations of multiple scattering by mineral aerosol particles in an atmosphere, since even unpolarized light becomes polarized after being scattered. Second, because different aerosol types have different polarization signatures, polarization measurements enhance the ability to observe the highly variable aerosol characteristics. Therefore polarimeters are included in a number of new remote sensing instruments such as POLDER and EOSP. These instruments have the retrieval of aerosol properties as a key objective, with emphasis on aerosol optical thickness [e.g., *Mishchenko and Travis*, 1997; *Bréon et al.*, 1997].

At present, little is known about the scattering matrices of mineral aerosols. In most cases it is assumed that the particles can be approximated by volume- or surface-equivalent spheres, so Lorenz-Mie calculations can be employed to determine their optical properties [e.g., *d'Almeida et al.*, 1991; *Bréon et al.*, 1997; *Moulin et al.*, 1997]. However, almost all mineral aerosols are irregular and the light-scattering properties of an ensemble of small irregular particles can differ significantly from those of an ensemble of spheres [e.g., *Bohren and Huffman*, 1983; *Mishchenko et al.*, 2000a]. This can have serious implications for the interpretation of satellite remote sensing data of nonspherical aerosol particles in the atmosphere, in particular for the retrieved aerosol optical thickness [*Mishchenko et al.*, 1995; *Herman et al.*, 1997; *Kahn et al.*, 1997].

Only a very limited number of scattering matrix measurements (laboratory or in situ) of mineral particles have been published. Measurements in the visible part of the spectrum using a large number of small particles falling through a light beam have been performed by several groups. All elements of the scattering ma-

trix have been measured, for example, for salt crystals [*Perry et al.*, 1978] and for quartz particles [*Holland and Gagne*, 1970; *Kuik et al.*, 1991; *Kuik*, 1992]. Other groups have measured a part of the scattering matrix (phase function and degree of linear polarization for incident unpolarized light), for example, for soil dust [*Jaggard et al.*, 1981] and for several kinds of irregular mineral particles [*West et al.*, 1997]. *Nakajima et al.* [1989] measured the phase function and some polarization properties in situ during a yellow sand event (dust storm) in Nagasaki.

Altogether, scattering matrix measurements are currently available for a limited number of samples of mineral particles and only for a few specific compositions, size distributions, and wavelengths.

In this paper we present measured scattering matrices as functions of the scattering angle at wavelengths of 441.6 nm and 632.8 nm for seven distinct aerosol samples with properties representative of the mineral aerosols present in the Earth's atmosphere. In this manner we try to obtain more insight in the differences and/or similarities of the scattering behavior of natural mineral aerosols with diameters roughly between 0.1 and 100 μm and a wide range in silicate composition.

To investigate the effects of irregular particles on light propagation through the atmosphere, information regarding scattering and extinction cross sections are required in addition to scattering matrices. However, laboratory measurements, in general, do not provide all these scattering properties, and certainly not for all types of aerosols occurring in the atmosphere. Therefore it is desirable to be able to compute these properties numerically [*Hill et al.*, 1984]. In addition, numerical calculations may help us to analyze the measured results, since the effect on light scattering of parameters, such as the refractive index, size, and shape of the aerosols, can then be studied independently and in detail.

Few numerical codes exist that can handle the irregularity and the size range required to analyze the measurements of the aerosol samples presented here [*Mishchenko et al.*, 2000a]. For instance, the discrete-dipole approximation (DDA) [*Draine*, 1988; *West*, 1991; *Lumme and Rahola*, 1994; *Draine*, 2000] can accommodate a wide variety of shapes, but calculations for particles with diameters larger than the wavelength are still too computer-time consuming.

The *T*-matrix method can, in principle, be used for larger particles than are attainable with DDA calculations [*Mishchenko and Travis*, 1998]. *Mishchenko et al.* [1997] argue that *T*-matrix calculations for randomly oriented spheroids, including a distribution in both axial ratios and size parameters, can describe the phase functions of mineral aerosol particles well [see also *Hill et al.*, 1984; *Mishchenko et al.*, 2000a]. However, this method is not yet feasible for most of the samples investigated in this paper [*Vermeulen*, 1999], since they contain large and irregular particles.

Here we present a pilot study in which we investigate whether a ray optics method, employing Gaussian random shapes [*Muinonen et al.*, 1996], can be used to interpret our measurements. The great advantage of this method is that one can take into account the irregular shape of the particles in a systematic way and in sufficient detail [*Muinonen*, 2000]. Furthermore, a similar ray optics method, including stochastic rough particles, has produced good agreement between calculated and measured phase functions and degrees of linear polarization for unpolarized incident light for certain specific irregular particles [*Peltoniemi et al.*, 1989; *Sasse and Peltoniemi*, 1995]. Finally, a number of published ray optics results for Gaussian random shapes show a promising resemblance to measured scattering matrices of irregular mineral particles [*Muinonen et al.*, 1996]. Thus despite the limitation that the ray optics approximation is, in principle, valid only for particle sizes much larger than the wavelength, we feel that the ray optics method, including Gaussian random shapes, is at present the most suitable method to analyze the measured results for most of the aerosol samples investigated here. However, we note that in this study our primary goal is to reproduce measured scattering matrices as functions of the scattering angle and not to derive aerosol properties.

In summary, we present the measured scattering matrices as functions of the scattering angle between 5° and 173° of seven aerosol samples relevant for studies of light scattering by mineral aerosols in general. In section 2 we characterize the seven aerosol samples. In section 3 we summarize the main concepts of light scattering applied. The experimental setup used to measure the scattering matrix elements is briefly described in section 4. In addition, the accuracy of the measurements and test results for water droplets are discussed in this section. In section 5 we present the measured scattering matrices as functions of the scattering angle for the various aerosol samples at two wavelengths. Furthermore, we compare the results for different aerosol samples and construct an average aerosol scattering matrix as a function of scattering angle. In section 6 we

present the results of ray optics calculations employing Gaussian random shapes and analyze the measured results. Finally, our results are discussed in section 7.

2. Characterization of the Aerosol Samples

In this section we discuss the properties of the aerosol samples that are most important as far as light scattering is concerned, i.e., particle size, particle shape, and the complex refractive index m. A brief characterization of each sample, including the effective radius, effective standard deviation of the radius, most abundant mineral constituents, real part of the refractive index, and color, is listed in Table 1. This will be discussed in the following sections:

2.1. Particle Sizes

There are several representations of the size distribution of a sample of small particles that are commonly used. For light-scattering purposes it is convenient to use a projected-surface-area distribution, because each particle scatters an amount of light proportional to the scattering cross-section GQ_{sca}. Here G is the geometrical cross section, and Q_{sca} is the scattering efficiency. Q_{sca} is approximately constant for irregular particles with diameters larger than ~ 1 μm and in visible light [e.g., *Bohren and Huffman*, 1983, Figure 11.20]. For the aerosol samples, projected surface-area distributions have been measured using a Fritsch laser particle sizer [*Konert and Vandenberghe*, 1997].

We define r as the radius of a sphere, called equivalent sphere, having the same projected surface area as the irregular particle has. Since the range in radii r is large, we plot normalized projected-surface-area distributions, i.e., $S(\log r)$, as functions of $\log r$, in the top panel in Figure 1 where r is expressed in micrometers. Here $S(\log r)d \log r$ gives the relative contribution by equivalent spheres with radii in the size range $\log r$ to $\log r + d \log r$ to the total projected surface per unit volume of space. This implies that equal areas under a

Table 1. Overview of Properties of the Aerosol Samples Studied

Sample	Main Constituents (Mineral or Mineral group)	r_{eff} (μm)	σ_{eff}	$Re(m)$	Color
Feldspar	K-feldspar, plagioclase, quartz	1.0	1.0	1.5-1.6	light pink
Red clay	biotite, illite, quartz	1.5	1.3	1.5-1.7	red brown
Quartz	quartz	2.3	1.5	1.54	white
Pinatubo volcanic ash	silica glass, plagioclase, amphibole, magnetite	3.0	3.5	1.5-1.7 2.1	light grey
Loess	K-feldspar, illite, quartz, calcite, chlorite, albite	3.9	1.6	1.5-1.7	yellow brown
Lokon volcanic ash	silica glass, plagioclase, magnetite	7.1	1.6	1.5-1.6 2.1	dark brown
Sahara sand	quartz, clay minerals, calcium carbonate	8.2	2.0	1.5-1.7	yellow brown
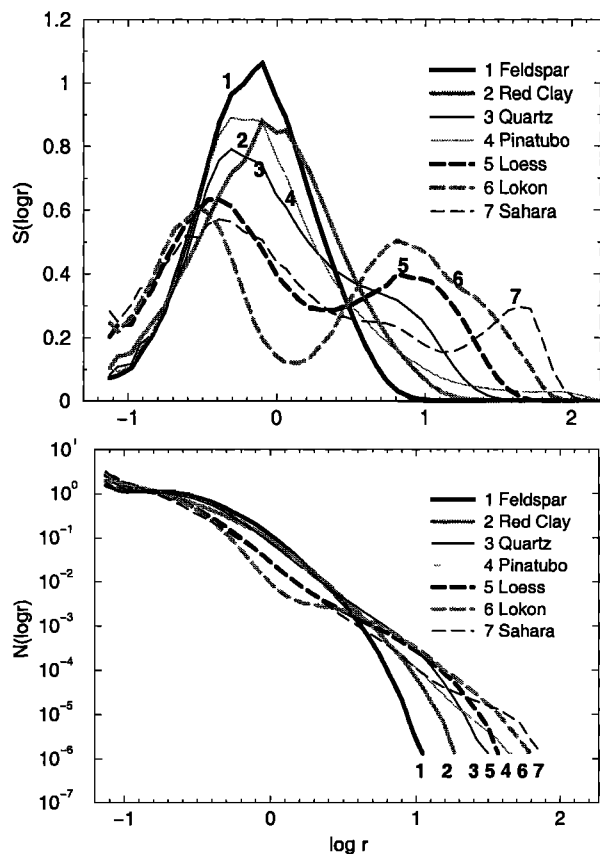
Figure 1. Measured normalized projected-surface-area distributions (top), and corresponding normalized number distributions (bottom), of the aerosol samples studied. The distributions are plotted as functions of log r, where r is expressed in micrometers.

curve correspond to equal contributions to the projected surface of all spheres per unit volume. The normalized projected-surface-area distributions are broad and partly overlap. Some of these distributions are bimodal, indicating that more than one principal size range may contribute to the scattering.

In addition, we plot normalized number distributions, $N(\log r)$, since these are often used in calculations and reported in the literature. In Figure 1 (bottom panel), $N(\log r)d \log r$ gives the relative contribution by equivalent spheres with radii in the size range log r to log r + $d \log r$ to the total number of equivalent spheres per unit volume of space. $N(\log r)$ was computed from the corresponding $S(\log r)$. For our experiments at least several grams of sample material were required. For this reason it was not feasible to work with aerosol particles collected directly from the atmosphere, because it is difficult to obtain enough particles in that manner. Therefore our samples originate from soil materials, which were either unprocessed (red clay, loess, Lokon volcanic dust, and Sahara sand) or which were processed to obtain a fine powder (feldspar, quartz, and Pinatubo volcanic ash). Nevertheless, comparison with the number distributions given, for example, by *d'Almeida et al.* [1991, Figure 4.1] shows that the normalized number

distributions of the mineral aerosol samples studied here are similar to those for mineral and dust-like aerosols found in the Earth's atmosphere.

To characterize our distributions with a few parameters, we calculated effective radii and standard deviations. The effective radius of a sample is defined as [*Hansen and Travis*, 1974]

$$r_{\text{eff}} = \frac{\int_0^\infty r\pi r^2 n(r)dr}{\int_0^\infty \pi r^2 n(r)dr}, \qquad (1)$$

where $n(r)dr$ is the fraction of the total number of equivalent spheres with radii between r and $r + dr$ per unit volume of space. Here $n(r)$ is readily computed from $N(\log r)$. Similarly, the effective standard deviation is defined as [*Hansen and Travis*, 1974]

$$\sigma_{\text{eff}} = \sqrt{\frac{\int_0^\infty (r - r_{\text{eff}})^2 \pi r^2 n(r)dr}{r_{\text{eff}}^2 \int_0^\infty \pi r^2 n(r)dr}}. \qquad (2)$$

The values for r_{eff} and σ_{eff} are listed in Table 1. The feldspar sample has the smallest effective radius (1.0 μm) and the Sahara sand the largest (8.2 μm). The Pinatubo sample has the largest σ_{eff}, namely 3.5. The other distributions have σ_{eff} values between 1.0 and 2.0. In the following we will consider the size of the particles relative to the wavelength of the scattered light; that is, the effective size parameter $x_{\text{eff}} = 2\pi r_{\text{eff}}/\lambda$.

2.2. Complex Refractive Indices

The mineral composition of the samples has been investigated by means of an electron microprobe (JEOL Ltd. JXA8800M) [*Reed*, 1993]. All elements were analyzed on wavelength-dispersive spectrometers, with 15 kV acceleration voltage and 25 nA probe current. Natural minerals and synthetic oxide compounds of well-known composition have been used as standards, and corrections for atomic weight, absorption and fluorescence were calculated with an on-line correction program. The irregular shape and inhomogeneity of the mineral aerosol particles cause considerable differences in the shape of the excitation volume, the length of the absorption path, and the secondary fluorescence. As a consequence, the resulting analyses can be regarded as qualitative only. The most abundant minerals or mineral groups obtained in this manner are given in Table 1. Also in this table, we provide a rough estimate of the range of the real part of the refractive indices of the samples, based on literature values for the main constituent minerals [*Kerr*, 1959; *Tröger et al.*, 1971; *Klein and Hurlbut*, 1993]. According to these authors, the wavelength dependence of $Re(m)$ is negligible over the visible range for the minerals listed in Table 1, with the exception of magnetite, which has $Re(m) \sim 2.1$. However, we emphasize that the samples studied consist of mixtures of minerals, so the $Re(m)$ values listed in Table 1, which pertain to the main individual miner-

als, may not be representative for the aerosol samples as a whole.

Egan and Hilgeman [1979] give values for the refractive indices of 24 natural soils over the visible part of the spectrum which occasionally are a little lower than the values for the bulk materials given in the references above. Notwithstanding, we may safely state that for most natural soils, values of $Re(m)$ are between 1.3 and 1.8 at visual wavelengths. Variations in $Re(m)$ are usually smaller than about 0.1 when going from λ=441.6 nm to 632.8 nm (the two wavelengths at which the measurements were performed). A notable exception are soils consisting predominantly of iron oxides, for which this variation can be up to 0.4 [*Egan and Hilgeman*, 1979]. In general, $Re(m)$ is larger in blue light than in red. We do not expect our samples to exhibit significant birefringence.

At a given wavelength the natural variability of $\text{Im}(m)$ within one mineral is at least 1 order of magnitude [*Gerber and Hindman*, 1982]. Therefore we just remark that for particles of crustal origin, such as our particles, $\text{Im}(m)$ is generally small, probably somewhere between 10^{-2} and 10^{-5} [*Egan and Hilgeman*, 1979; *Gerber and Hindman*, 1982]. Also, the dependence of $\text{Im}(m)$ on wavelength is highly variable, in particular in the visible, due to the presence of trace elements, such as iron and chromium. When iron is present, $\text{Im}(m)$ is usually larger for 441.6 nm than for 632.8 nm [*Egan and Hilgeman*, 1979; *Deepak*, 1982]. For some clays the difference in $\text{Im}(m)$ for the two wavelengths can be up to a factor of 4 and for iron-rich soils even up to a factor of 10 [*Egan and Hilgeman*, 1979].

2.3. Particle Shapes

Examples of particle shapes are shown in the scanning electron microscope (SEM) photographs displayed in Figure 2. The feldspar particles as well as the quartz particles exhibit angular shapes. The red clay particles show layered structures, while the Sahara sand particles as well as the loess particles are rounded, because of wind erosion. The Sahara sand sample mainly consists of quartz particles coated with other minerals. The volcanic ashes have a wide variety of shapes, varying from long, thin cylindrical, and angular to rounded shapes. In all samples, even single particles may exhibit a lot of structure (see bottom right panel in Figure 2).

In short the samples consist of particles that have irregular and diverse shapes; we call such samples irregular samples. In addition, the particles in the samples are diverse in size, and most of them (except for the quartz particles) are inhomogeneous in composition and therefore in complex refractive index.

3. Some Concepts of Light-Scattering Theory

We summarize here the main concepts of light-scattering theory used in this paper. The flux and polar-

ization of a quasi-monochromatic beam of light can be represented by a column vector $\mathbf{I} = \{I, Q, U, V\}$, the so-called Stokes vector [*van de Hulst*, 1957, section 5.12; *Hovenier and van der Mee*, 1983]. The Stokes parameter I is proportional to the total flux of the beam. The Stokes parameters Q and U represent differences between two components of the flux for which the electric field vectors oscillate in orthogonal directions. The Stokes parameter V is the difference between two oppositely circularly polarized components of the flux. A plane through the direction of propagation of the beam is chosen as a plane of reference for the Stokes parameters.

If light is scattered by a sample of randomly oriented particles and time reciprocity applies, as is the case in our experiment, the Stokes vectors of the incident beam and the scattered beam are related by a 4×4 scattering matrix, for each scattering angle θ, as follows [*van de Hulst*, 1957, section 5.22]:

$$\begin{pmatrix} I_{sc} \\ Q_{sc} \\ U_{sc} \\ V_{sc} \end{pmatrix} = \frac{\lambda^2}{4\pi^2 D^2} \begin{pmatrix} F_{11} & F_{12} & F_{13} & F_{14} \\ F_{12} & F_{22} & F_{23} & F_{24} \\ -F_{13} & -F_{23} & F_{33} & F_{34} \\ F_{14} & F_{24} & -F_{34} & F_{44} \end{pmatrix} \begin{pmatrix} I_{in} \\ Q_{in} \\ U_{in} \\ V_{in} \end{pmatrix}, \quad (3)$$

where the subscripts in and sc refer to the incident and scattered beams, λ is the wavelength, and D is the distance from the sample to the detector. The matrix $\mathbf{F}$ with elements F_{ij}, is called the scattering matrix. Its elements depend on the scattering angle but not on the azimuthal angle. Here the plane of reference is the scattering plane, i.e., the plane containing the incident and the scattered light. The elements $F_{ij}(\theta)$ contain information about the size relative to the wavelength, shape, and complex refractive index of the scatterers. It follows from equation (3) that there are 10 matrix elements to be determined. This number is further reduced in case a scattering sample consists of randomly oriented particles with equal amounts of particles and their mirror particles. The four elements $F_{13}(\theta)$, $F_{14}(\theta)$, $F_{23}(\theta)$, and $F_{24}(\theta)$ are then zero over the entire angle range [*van de Hulst*, 1957]. For convenience, we normalize all matrix elements (except $F_{11}(\theta)$ itself) to $F_{11}(\theta)$; that is, we consider $F_{ij}(\theta)/F_{11}(\theta)$, with $i, j = 1$ to 4.

For unpolarized incident light, $F_{11}(\theta)$ is proportional to the flux of the scattered light and is also called scattering function or phase function. For reasons of convenience and tradition, a minus sign is often written in front of $F_{12}(\theta)/F_{11}(\theta)$. Thus we use

$$-F_{12}(\theta)/F_{11}(\theta) = \frac{I_\perp(\theta) - I_\parallel(\theta)}{I_\perp(\theta) + I_\parallel(\theta)}, \quad (4)$$

where for unpolarized incident light $I_\perp(\theta)$ and $I_\parallel(\theta)$ represent the flux of the scattered light polarized perpendicular and parallel to the plane of reference. The ratio $-F_{12}(\theta)/F_{11}(\theta)$ equals the degree of linear polarization
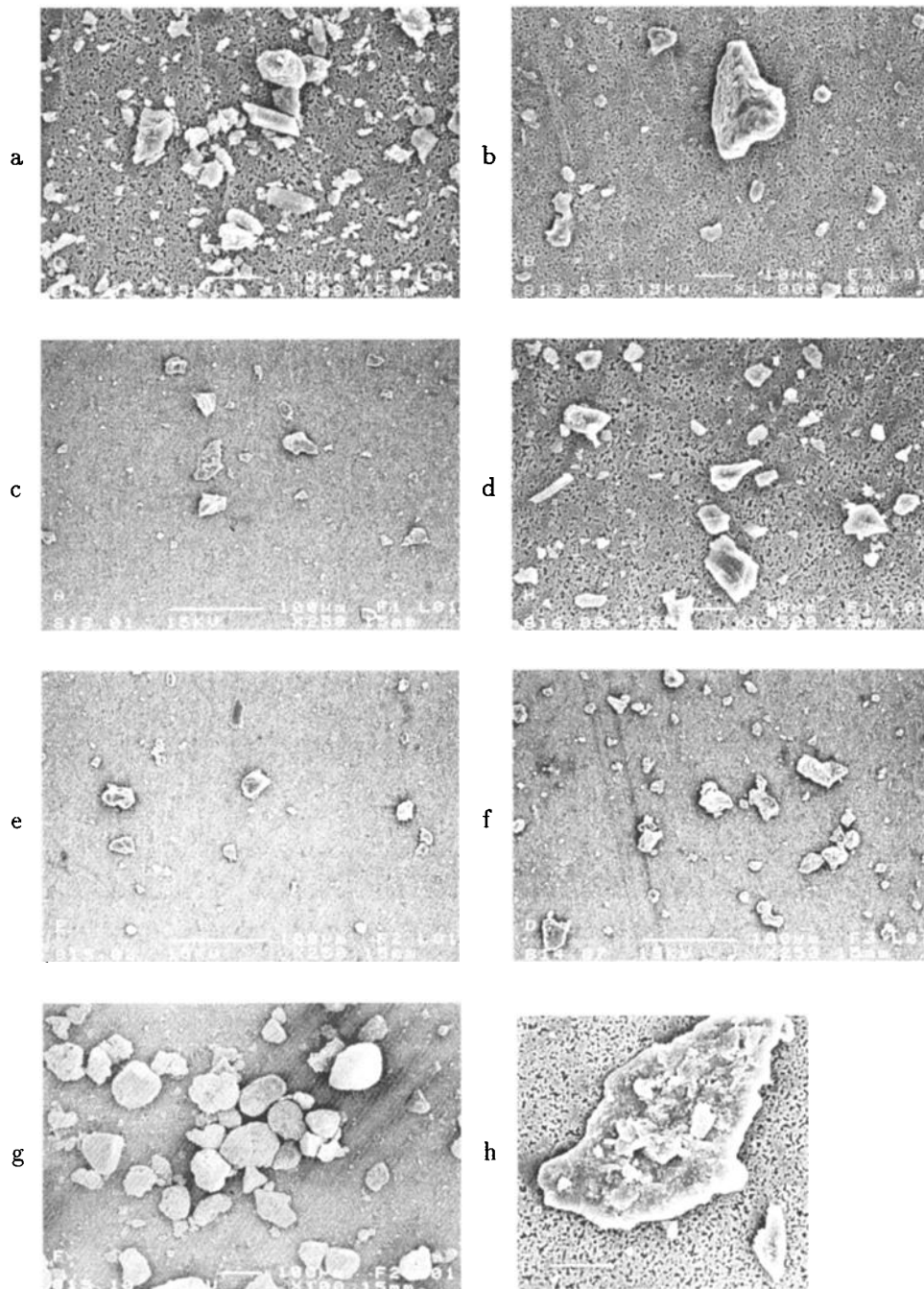
Figure 2. Scanning electron microscope (SEM) photographs of the aerosol samples studied: (a) feldspar, (b) red clay, (c) quartz, (d) Pinatubo ash, (e) loess, (f) Lokon ash, and (g) Sahara sand. An example of irregularity of a single (quartz) particle is shown in photograph Figure 2h. White bars in Figures 2a, 2b, 2d, and 2h denote 10 μm but in the remaining photographs, 100 μm.

of the scattered light if the incident light is unpolarized and $F_{13}(\theta) = 0$. Note further that we must have $|F_{ij}(\theta)/F_{11}(\theta)| \leq 1$ [see *Hovenier et al.*, 1986].

In addition, the matrix elements should satisfy the Cloude (coherency matrix) test as described by *Hovenier and van der Mee* [1996]. The reliability of scattering matrix measurements can be investigated by applying this test, i.e., one checks whether each measured matrix at each measured angle can be a sum of pure scattering matrices. In principle, this test can be used only for matrices of which all elements have been de-

termined. However, it is sometimes convenient to skip measuring one or more of the elements $F_{13}(\theta)$, $F_{14}(\theta)$, $F_{23}(\theta)$, and $F_{24}(\theta)$. In such cases we apply the Cloude test, assuming that each skipped element is zero.

4. Experimental Method

In this section we give a brief description of the experimental setup, the accuracy of the measurements, and the results of test measurements on water droplets.
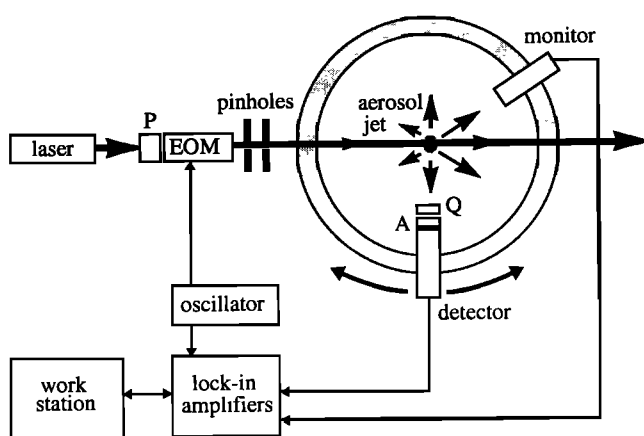
Figure 3. Schematic picture of the experimental setup; P, polarizer; A, polarization analyzer; Q, quarter-wave plate; EOM, electro-optic modulator.

4.1. Experimental Setup

The experimental setup used to measure the scattering matrix elements of the aerosol samples is shown in Figure 3. The setup is similar to that developed by *Hunt and Huffman* [1973] and is a revised and improved version of that described by *Stammes* [1989], *Kuik et al.* [1991], and *Kuik* [1992]. Here we briefly summarize the main characteristics of the setup. A more comprehensive description can be found in the work of *Hovenier* [2000].

Light from a linearly polarized continuous wave He-Ne laser ($\lambda = 632.8$ nm, 5 mW) or He-Cd laser ($\lambda = 441.6$ nm, 40 mW) passes through a polarizer oriented at an angle γ_P and an electro-optic modulator oriented at an angle γ_M (angles of optical elements are angles between their optical axes and the reference plane, measured counterclockwise when looking in the direction of propagation of the light). The modulated light is subsequently scattered by randomly oriented particles located in a jet stream produced by an aerosol generator. The scattered light passes through a quarter-wave plate oriented at an angle γ_Q and an analyzer oriented at an angle γ_A (both optional) and is detected by a photomultiplier tube that moves along a ring in steps of 5°, or steps of 1° if a higher angular resolution is required.

The detector covers a scattering angle range from 5° (nearly forward scattering) to 173° (nearly backward scattering). The field of view of the detector is ~ 2°, which is sufficiently large to ensure that the detector sees the entire illuminated part of the aerosol jet at all scattering angles. The monitor is a photomultiplier tube placed at a fixed angle and is used to correct for variations in the aerosol stream.

The modulator in the setup, in combination with lock-in detection, increases the accuracy of the measurements and allows determination of several elements of the scattering matrix from the detector signal. For this purpose, a voltage varying sinusoidally in time is applied to the modulator crystal. The phase shift between the parallel and the perpendicular components of the electric field caused by the crystal is also sinusoidal, so the sine and cosine of the resulting phase shift can be described by Bessel functions of the first kind $J_k(x)$. If the amplitude ϕ_0 of the varying phase shift is chosen appropriately, the flux reaching the detector is [*Hovenier*, 2000]

$$I_{\text{det}}(\theta) = c[DC(\theta) + 2J_1(\phi_0)S(\theta)\sin \omega t$$

$$+2J_2(\phi_0)C(\theta)\cos 2\omega t + ...], \tag{5}$$

where $J_1(\phi_0)$ and $J_2(\phi_0)$ are known constants, and c is a constant that depends on the optical arrangement. The modulation angular frequency ω is 1 kHz. The coefficients $DC(\theta)$, $S(\theta)$, and $C(\theta)$ contain elements of the scattering matrix (see Table 2) [e.g., *Kuik*, 1992; *Hovenier*, 2000]. Note that $F_{11}(\theta)$ is measured only on a relative scale in our experiments. By using lock-in detection the constant part of the detector signal containing $cDC(\theta)$ and each of the varying parts containing $cS(\theta)$ and $cC(\theta)$ are separated. Subsequently, we divide $cS(\theta)$ and $cC(\theta)$ by $cDC(\theta)$, belonging to the same configuration, which eliminates c for these ratios. We use $F_{12}(\theta)/F_{11}(\theta)$, $F_{13}(\theta)/F_{11}(\theta)$, and $F_{14}(\theta)/F_{11}(\theta)$, which are measured directly with configurations 1 and 5 in Table 2, to obtain the other element ratios measured with configurations 2, 3, 4, 6, 7, and 8. For example, from configuration 2 and the relation

Table 2. Configurations of the Orientation Angles, γ_P, γ_M, γ_Q, and γ_A; of the Polarizer, the Modulator, the Quarter-Wave Plate, and the Analyzer Used During the Measurements[a]

Configuration	γ_P	γ_M	γ_Q	γ_A	$DC(\theta)$	$S(\theta)$	$C(\theta)$
1	0°	-45°	–	–	F_{11}	$-F_{14}$	F_{12}
2	0°	-45°	–	0°	$F_{11} + F_{12}$	$-F_{14} - F_{24}$	$F_{12} + F_{22}$
3	0°	-45°	–	45°	$F_{11} - F_{13}$	$-F_{14} - F_{34}$	$F_{12} - F_{23}$
4	0°	-45°	0°	45°	$F_{11} + F_{14}$	$-F_{14} - F_{44}$	$F_{12} + F_{24}$
5	45°	0°	–	–	F_{11}	$-F_{14}$	F_{13}
6	45°	0°	–	0°	$F_{11} + F_{12}$	$-F_{14} - F_{24}$	$F_{13} + F_{23}$
7	45°	0°	–	45°	$F_{11} - F_{13}$	$-F_{14} - F_{34}$	$F_{13} + F_{33}$
8	45°	0°	0°	45°	$F_{11} + F_{14}$	$-F_{14} - F_{44}$	$F_{13} - F_{34}$

[a]The coefficients $DC(\theta)$, $S(\theta)$, and $C(\theta)$ correspond to the dc, $\sin \omega t$, and $\cos \omega t$ component of the detector signal, respectively.
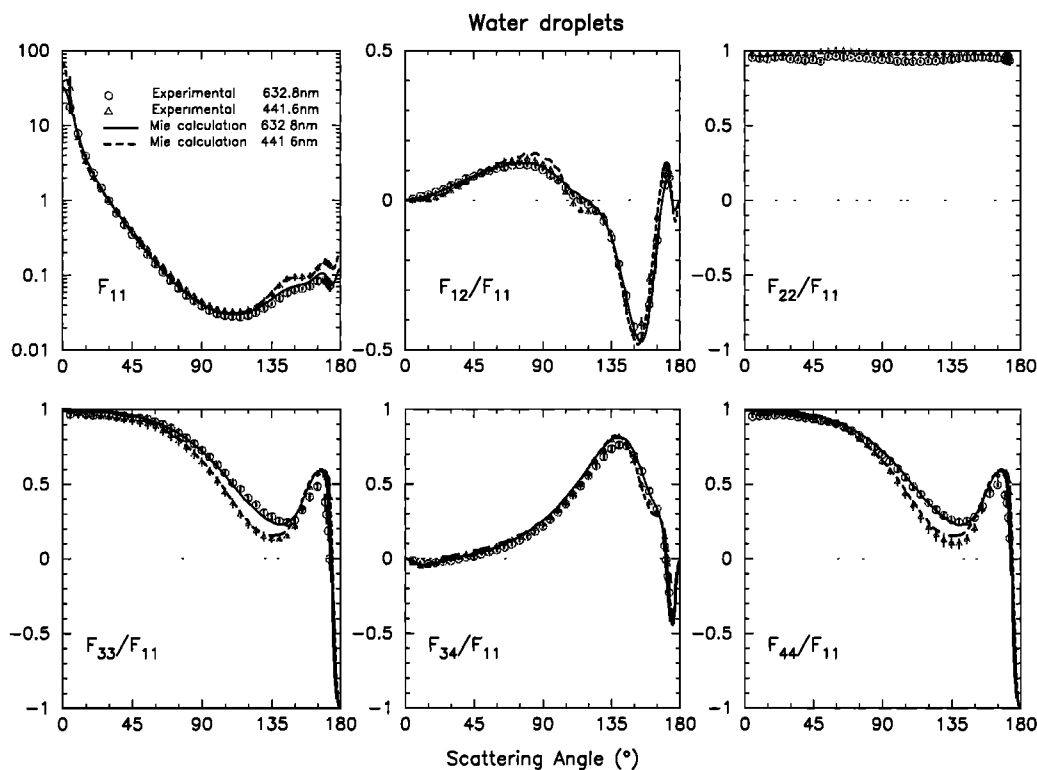
Figure 4. Scattering matrix elements $F_{11}(\theta)$, normalized to 1 at 30° and element ratios $F_{12}(\theta)/F_{11}(\theta)$, $F_{22}(\theta)/F_{11}(\theta)$, $F_{33}(\theta)/F_{11}(\theta)$, $F_{34}(\theta)/F_{11}(\theta)$, and $F_{44}(\theta)/F_{11}(\theta)$ for water droplets. Circles denote the measurements at 632.8 nm, triangles those at 441.6 nm, together with their error bars. Solid and dashed lines are results of Lorenz-Mie calculations for 632.8 nm and 441.6 nm, respectively.

$$\frac{F_{14}(\theta) + F_{24}(\theta)}{F_{11}(\theta) + F_{12}(\theta)} = \frac{\frac{F_{14}(\theta)}{F_{11}(\theta)} + \frac{F_{24}(\theta)}{F_{11}(\theta)}}{1 + \frac{F_{12}(\theta)}{F_{11}(\theta)}} \qquad (6)$$

we can calculate $F_{24}(\theta)/F_{11}(\theta)$, since it is the only unknown in this equation. Other element ratios are determined in a similar way.

4.2. Accuracy of the Measurements

For each data point at a given scattering angle, 720 measurements are conducted in about 2 s. Consequently, one single data point is in fact an average of 720 separate measurements. In the case that there was just one data point per angle for a given scattering matrix element or combinations of matrix elements (e.g., because of the limited amount of the sample available), the adopted error is due to the variation of the signal during the single series of 720 measurements. However, in most cases the values obtained for the measured matrix elements or combinations of matrix elements are the mean value of several data points (about 5 or more) and the adopted experimental error is the standard deviation of this mean value. When a matrix element ratio is not measured directly but is obtained using equation (6) or a similar equation, its standard deviation is calculated

from standard deviations of the directly measured matrix elements or combinations of matrix elements. The resulting experimental errors are indicated by error bars in Figure 4 and in later figures containing experimental results. When no error bar is visible, the value of the standard deviation is smaller than the symbol plotted.

In a few cases the error bars are large, for example, for the Sahara sand sample. This is predominantly due to the fact that the particles in these samples are relatively large so that relatively few particles are present in the scattering volume during the measurements, thereby decreasing the signal-to-noise ratio. An increase in the jet flow would have improved the accuracy, but this was not possible because of the limited amount of sample material available.

We investigated the reliability of the measurements presented in this paper by applying the Cloude coherency test [*Hovenier and van der Mee*, 1996] (see section 3). For a few samples, we had not enough sample material to measure $F_{23}(\theta)/F_{11}(\theta)$ (loess) or both $F_{13}(\theta)/F_{11}(\theta)$ and $F_{23}(\theta)/F_{11}(\theta)$ (Sahara sand). To be able to apply the Cloude coherency test for these samples, we assumed these elements to be zero at all scattering angles, since they proved to be identically zero within the experimental errors for the other samples.

We found that for all matrices, the values that measured for scattering angles from 5° to 173° satisfy the Cloude test within the experimental error.

4.3. Test Measurements Using Water Droplets

We have tested the experimental setup by comparing results of water droplet measurements at 441.6 nm and 632.8 nm to results of Lorenz-Mie calculations [*Mie,* 1908] for homogeneous spherical particles. The water droplets were produced by a nebulizer. For the Lorenz-Mie calculations we used a lognormal number distribution having $r_{eff} = 1.1$ μm, $\sigma_{eff} = 0.5$ [see *Hansen and Travis,* 1974], and a refractive index $m = 1.33 - i0.00$. Since the values for r_{eff} and σ_{eff} of the water droplets were not known, they were chosen so that the differences between measured and calculated scattering matrix elements as a function of scattering angle were minimized.

The results of the $F_{11}(\theta)$ measurements and calculations are plotted on a logarithmic scale in Figure 4. We chose to normalize the measured and calculated $F_{11}(\theta)$ so that it is equal to 1 at $\theta = 30°$. The other elements shown in Figure 4 were plotted relative to $F_{11}(\theta)$. We refrained from showing the four element ratios $F_{13}(\theta)/F_{11}(\theta)$, $F_{14}(\theta)/F_{11}(\theta)$, $F_{23}(\theta)/F_{11}(\theta)$, and $F_{24}(\theta)/F_{11}(\theta)$, since we verified that these ratios do not differ from zero by more than the error bars, as is in accordance with Lorenz-Mie theory.

When the results of the water droplet measurements are compared with the results of Lorenz-Mie calculations (see Figure 4), we find that there is good agreement over the entire angle range for most scattering matrix elements. Note that the measured ratios $F_{33}(\theta)/F_{11}(\theta)$ and $F_{44}(\theta)/F_{11}(\theta)$ are found to be identical, which is in accordance with Lorenz-Mie theory. The largest systematic deviation from Lorenz-Mie theory, albeit only of a few percent, is found for $F_{22}(\theta)/F_{11}(\theta)$. This may be due to an accumulation of small alignment errors in the experiment [*Kiphardt,* 1993]. We note that systematic errors, for example due to small inaccuracies in the alignment of the optical elements, are not accounted for in the error bars.

5. Measured Scattering Matrices of Mineral Aerosol Particles

In section 5.1 we present the experimentally determined scattering matrices for the seven aerosol samples described in section 2. An intercomparison of the results for the various samples is made in section 5.2. In section 5.3 we construct an average scattering matrix as a function of scattering angle. A more detailed discussion of the results is given in section 7.

5.1. Measurements

We present in Figures 5–11 results of the experimentally determined scattering matrices at 441.6 nm and 632.8 nm as a function of the scattering angle θ for the aerosol samples feldspar, red clay, quartz, Pinatubo volcanic ash, loess, Lokon volcanic ash, and Sahara sand. These figures also contain results of ray-optics calculations that will be discussed in section 6.

All $F_{11}(\theta)$ functions are plotted on a logarithmic scale. They are normalized so that they equal 1 at $\theta = 30°$. The other elements are shown relative to the corresponding $F_{11}(\theta)$. Measurements were performed at intervals of 5° for θ in the range 5° − 170° and at intervals of 1° for θ from 170° to 173°. As for the water droplets, we refrained from plotting the four element ratios $F_{13}(\theta)/F_{11}(\theta)$, $F_{14}(\theta)/F_{11}(\theta)$, $F_{23}(\theta)/F_{11}(\theta)$, and $F_{24}(\theta)/F_{11}(\theta)$, since we verified that these ratios do not differ from zero by more than the error bars. This is in agreement with the assumption that our samples consist of randomly oriented particles with equal numbers of particles and their mirror particles [*van de Hulst,* 1957]. Consequently, we will interpret $-F_{12}(\theta)/F_{11}(\theta)$ as the degree of linear polarization for unpolarized incident light.

### 5.2. Intercomparison of the Aerosol Scattering Matrices

Comparison of the results for the seven samples reveals several fundamental and important aspects of the scattering matrix elements of mineral aerosols in general. In this section we focus on (1) the main common properties of the scattering matrices, (2) the dependence on particle size and complex refractive index, and (3) the wavelength dependence of the scattering matrix elements. A more detailed discussion will be given in section 7.

In all cases the $F_{11}(\theta)$ curves measured are smooth functions of the scattering angle, showing a steep forward peak and virtually no structure at sidescattering and backscattering angles. The shapes are similar for all aerosol samples and are in agreement with the general behavior exhibited by nonspherical particles [*Mishchenko et al.,* 2000b]. The steepness of the $F_{11}(\theta)$ curves, defined as the measured maximum value of $F_{11}(\theta)$ divided by the measured minimum value over the scattering angle range from 5° to 173°, varies from ∼400 to ∼60 (see Figure 12, top panel). Such differences in steepness may be important, since, for example, they can result in an underestimation or overestimation of the optical thickness of mineral aerosols when phase functions with incorrect steepness are used for the interpretation of satellite reflectance measurements [*Mishchenko et al.,* 1996a; *Kahn et al.,* 1997].

The steepness of $F_{11}(\theta)$ depends strongly on the effective size parameter of the irregular particles. Figure 12 shows that the steepest curves occur for the smallest particles, i.e., red clay and feldspar. The flattest $F_{11}(\theta)$ curves occur for the largest particles, i.e., Lokon vol-
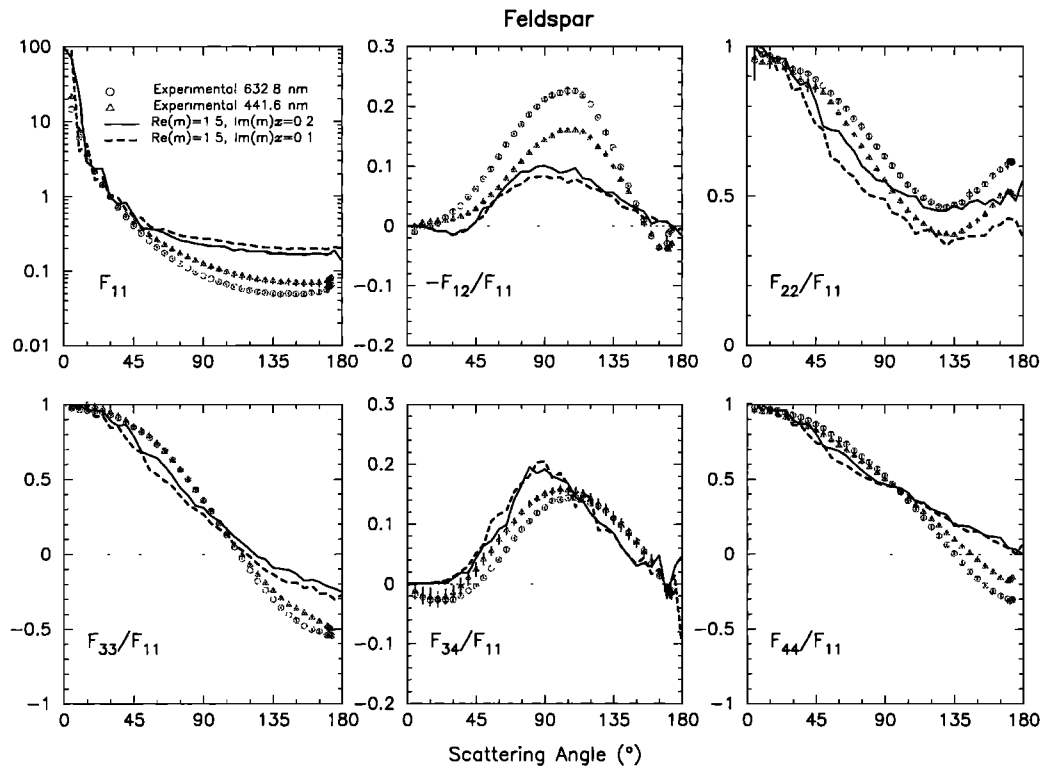
Figure 5. Scattering matrix elements $F_{11}(\theta)$, normalized to 1 at 30° and element ratios $-F_{12}(\theta)/F_{11}(\theta)$, $F_{22}(\theta)/F_{11}(\theta)$, $F_{33}(\theta)/F_{11}(\theta)$, $F_{34}(\theta)/F_{11}(\theta)$, and $F_{44}(\theta)/F_{11}(\theta)$ for feldspar. Circles denote the measurements at 632.8 nm, triangles those at 441.6 nm, together with their error bars. Results of geometric-optics calculations for Gaussian random particles with $\Gamma=5°$, and $\sigma = 0.2$, are indicated by solid and dashed lines, corresponding to comparisons with measured results for 632.8 nm and 441.6 nm, respectively (see section 6).
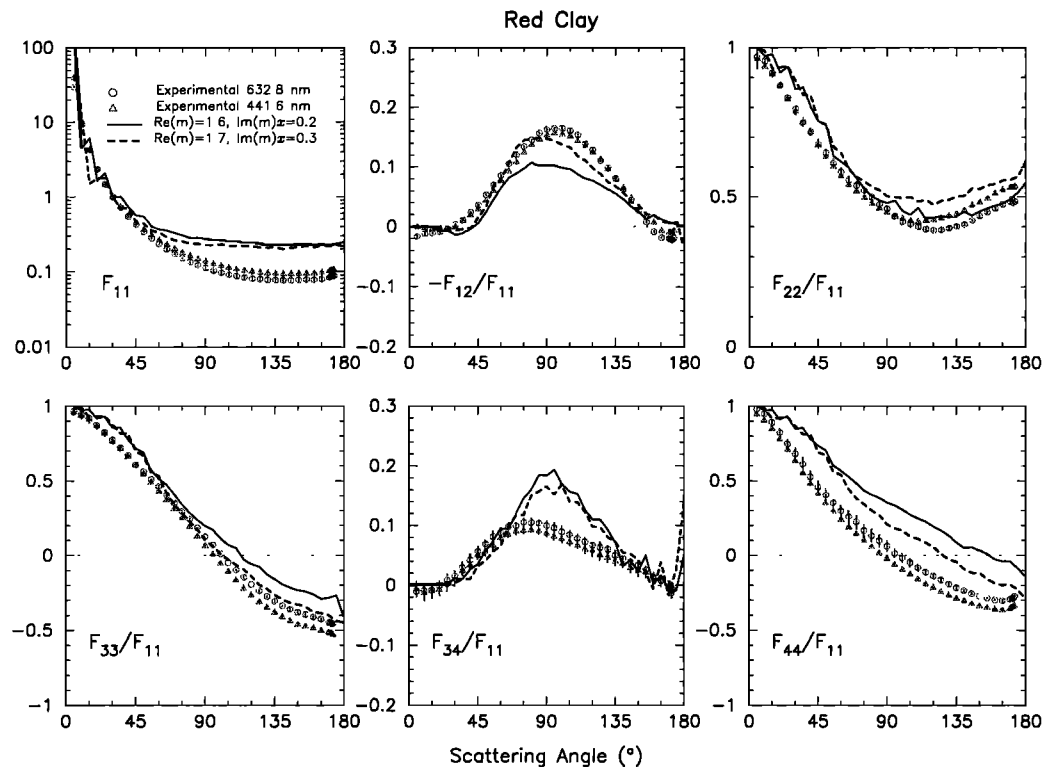
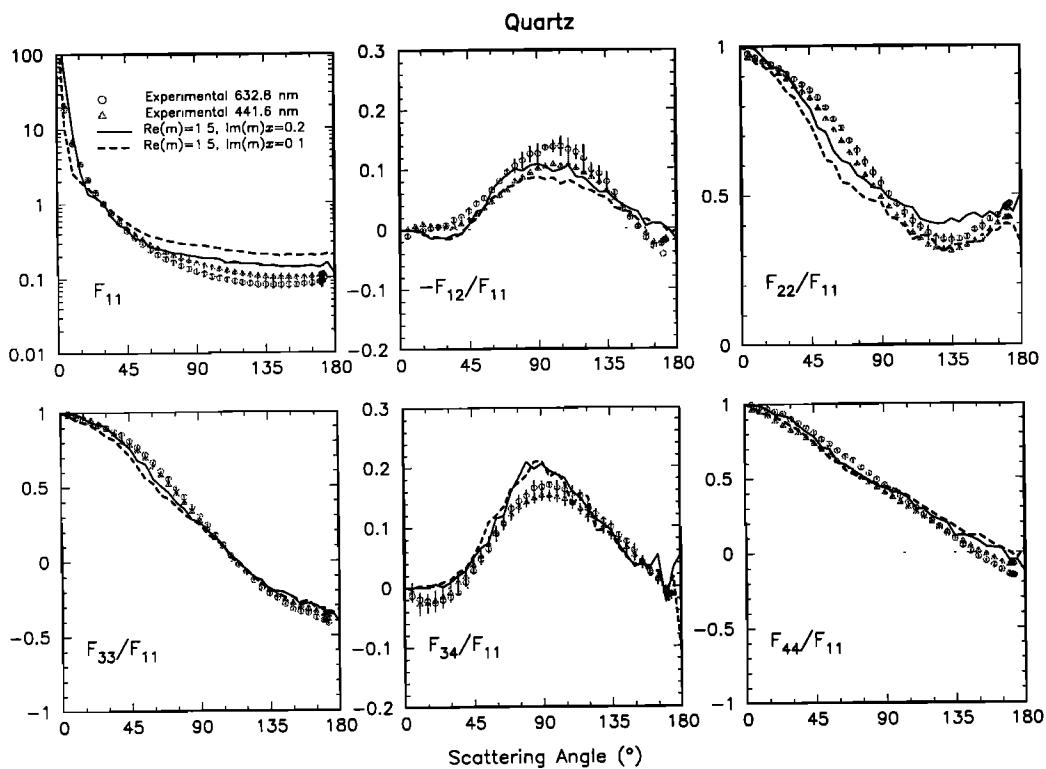**Figure 6.** Same as Figure 5 but for red clay.

Quartz

Figure 7. Same as Figure 5 but for quartz.
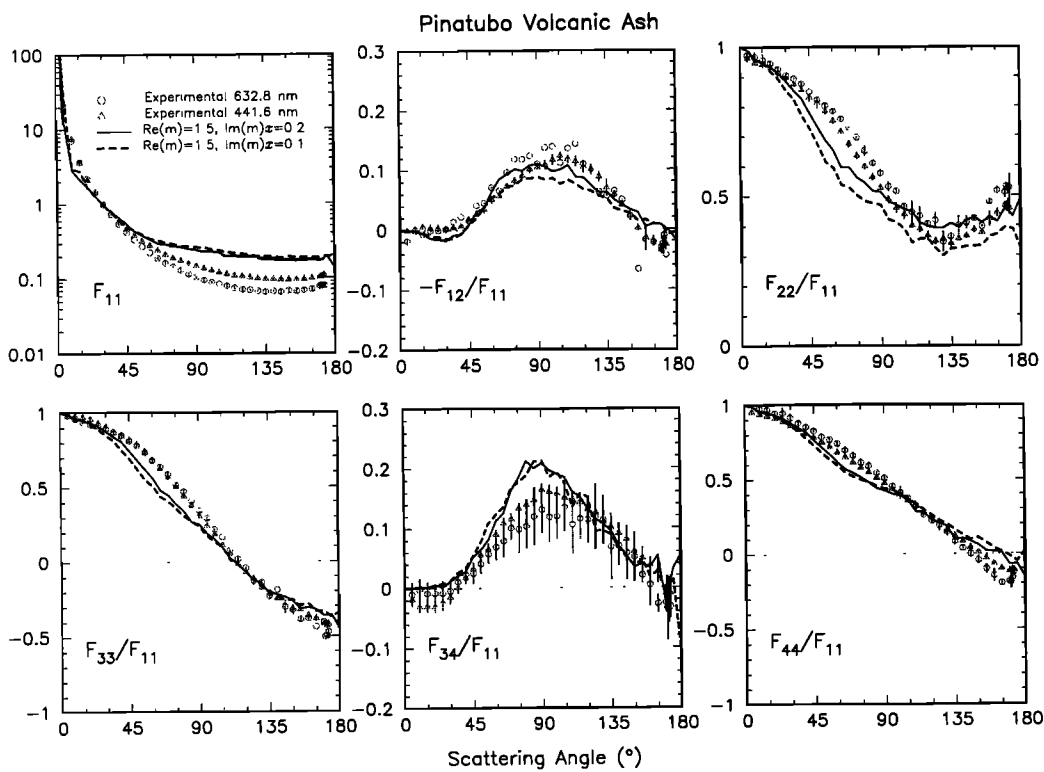
Pinatubo Volcanic Ash

Figure 8. Same as Figure 5 but for Pinatubo volcanic ash.
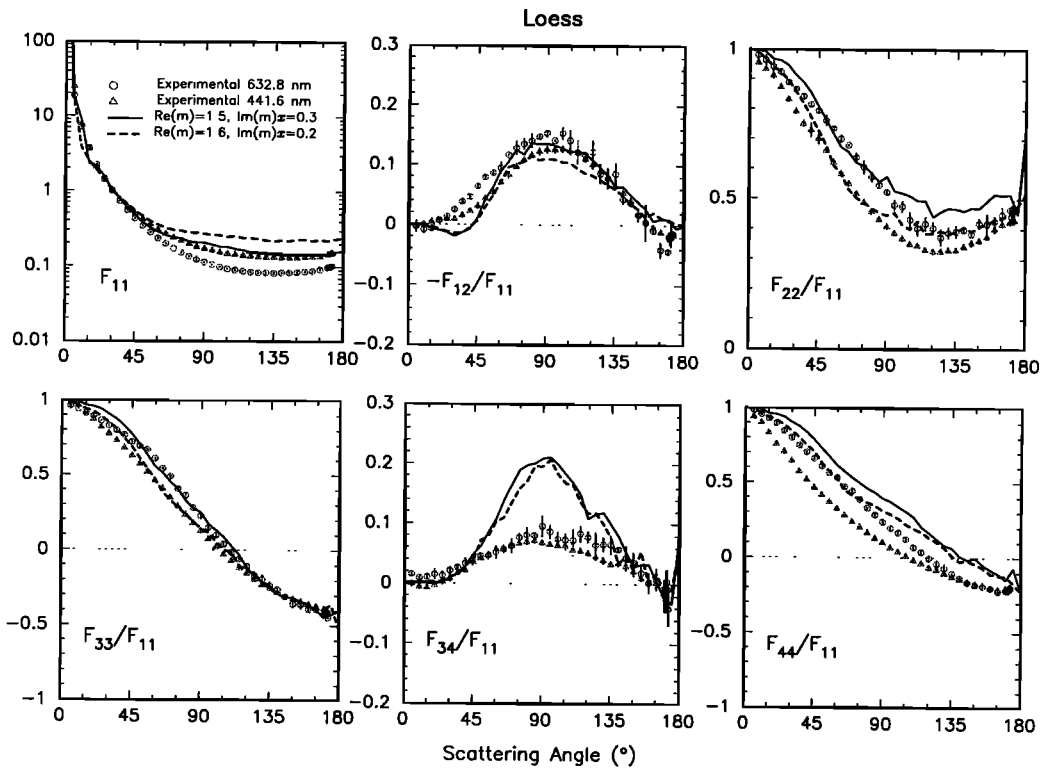
Loess

Figure 9. Same as Figure 5 but for loess.
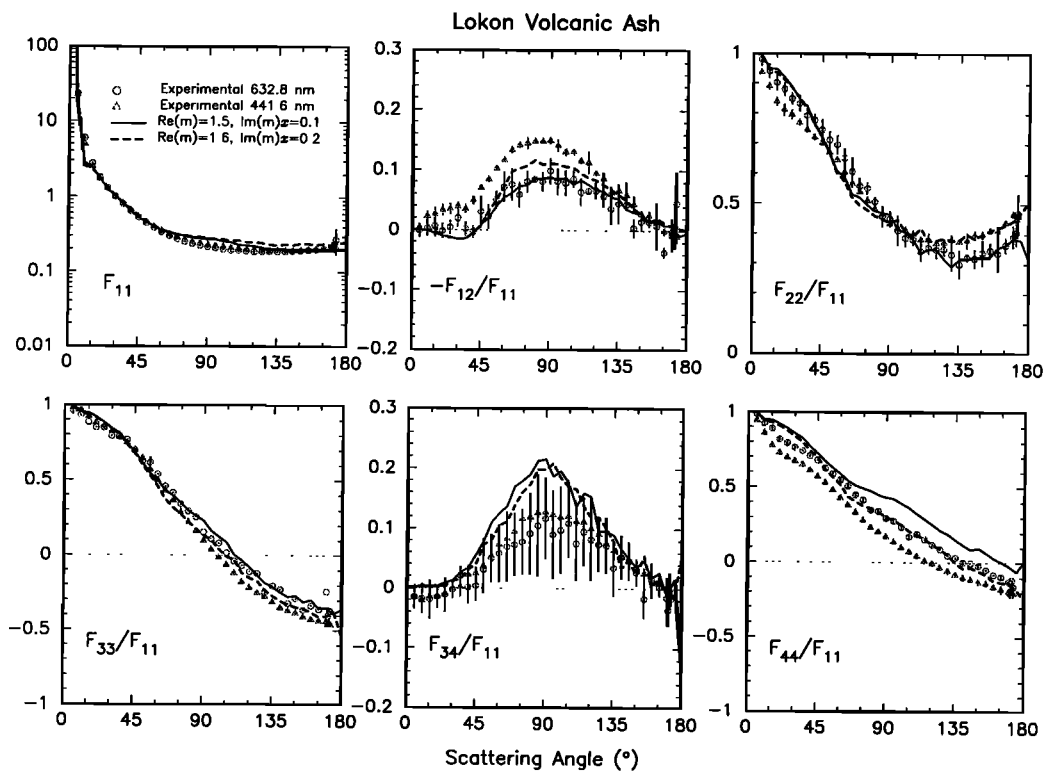
Lokon Volcanic Ash

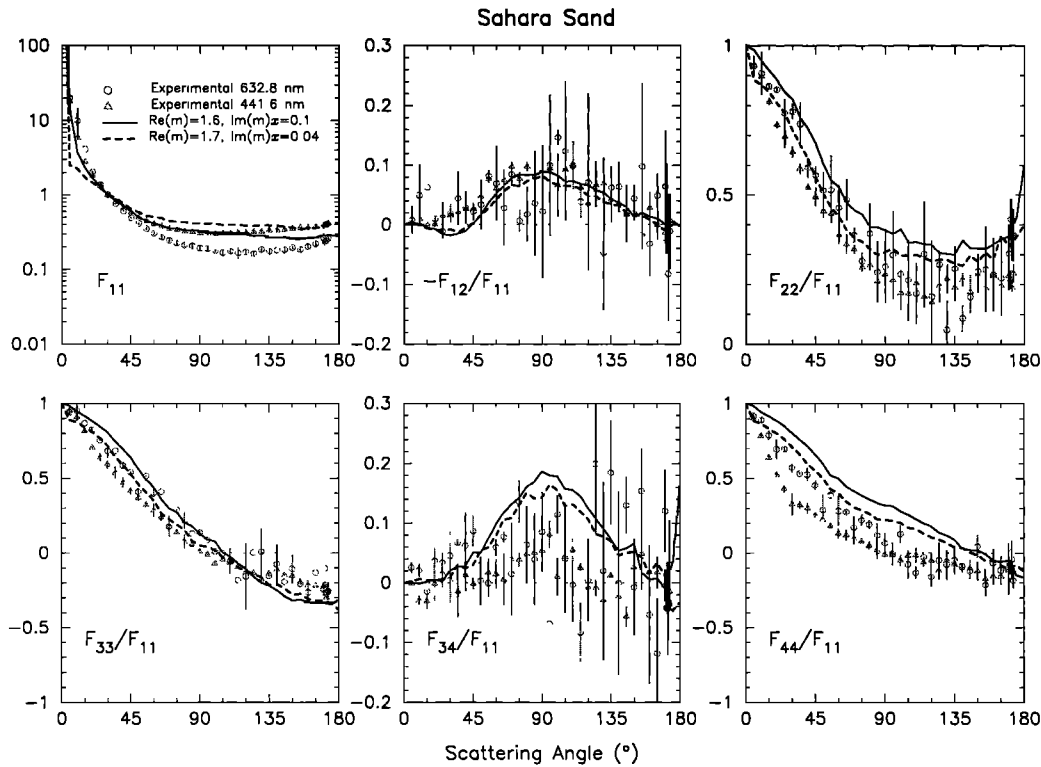**Figure 10.** Same as Figure 5 but for Lokon volcanic ash.

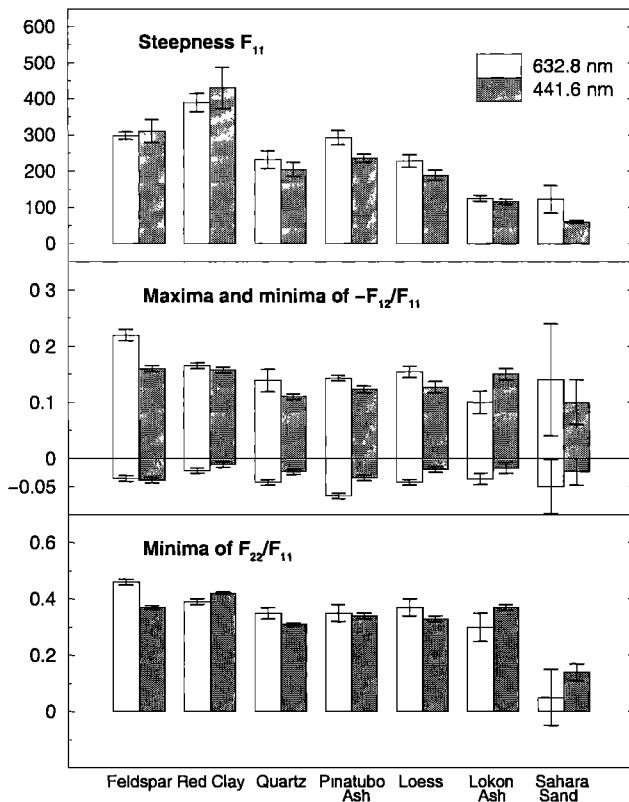**Figure 11.** Same as Figure 5 but for Sahara sand.

Figure 12. Properties of the measured scattering matrix elements. (top) Steepnesses of $F_{11}(\theta)$, at $\lambda=632.8$ nm and 441.6 nm. (middle) Maximum and minimum measured values of $-F_{12}(\theta)/F_{11}(\theta)$. (bottom) Minimum measured values of $F_{22}(\theta)/F_{11}(\theta)$. The samples are arranged horizontally according to increasing values of r_{eff}. Error bars are also shown.

canic ash and Sahara sand. We note that the measurements do not include forward diffraction peaks for angles smaller than 5°. Forward diffraction peaks are generally steeper for large particles than for small particles. However, over the angle range measured here, the diffraction peaks apparently hardly influence the steepness. Apart from the size parameter, the complex refractive index is probably important in determining the steepness. For example, the dark-colored red clay shows a larger steepness of $F_{11}(\theta)$ than the smaller and light-colored feldspar particles. Similar behavior indicating the influence of the effective size parameter and complex refractive index is observed if we consider the full shapes of $F_{11}(\theta)$ (see Figures 5-11). The curves for side and backward scattering between 30° and 173° are flatter at 441.6 nm than at 632.8 nm for all samples except the dark-colored Lokon ash.

The measured $-F_{12}(\theta)/F_{11}(\theta)$ curves are all found to be similar in shape. These curves display a maximum at side-scattering angles and lie below zero beyond around 160°. The maximum and minimum values measured have been plotted in Figure 12 (middle panel). For Sahara sand at 632.8 nm, where the uncertainty in the measured values was very large, the minimum value is an average of the measured values at 172° and 173°.

As in the case of the phase function, $F_{11}(\theta)$, the information displayed in Figures 5-11 about the degree of linear polarization for unpolarized incident light, $-F_{12}(\theta)/F_{11}(\theta)$, of mineral aerosols may improve the interpretation of satellite data [e.g., *Herman et al.*, 1997] (see section 7). To explain the behavior of the maxima of $-F_{12}(\theta)/F_{11}(\theta)$, we consider the following:

If geometric optics applies (i.e., if the size of the scatterer is much larger than the incident wavelength) and $Im(m)$ is not zero, both an increase in the size parameter of the particles and an increase in $Im(m)$ will result in a larger absorption, causing the maximum of $-F_{12}(\theta)/F_{11}(\theta)$ to go up. However, the maximum of $-F_{12}(\theta)/F_{11}(\theta)$ will increase also if the particles become small enough, since eventually, in the Rayleigh domain (i.e., for particles much smaller than the wavelength), $-F_{12}(\theta)/F_{11}(\theta)$ will reach a maximum of one at 90°.

In our case, the samples have broad projected-surface-area distributions that overlap both size regions (particles with sizes smaller or comparable to the wavelength and sizes much larger than the wavelength). The percentage of projected-surface area corresponding to spheres with radii smaller than 1 μm (Figure 1) is for most samples rather high. Figure 12 (middle panel) shows that $-F_{12}(\theta)/F_{11}(\theta)$ tends to show larger maxima for smaller values of x_{eff}. For example, when going from 441.6 nm to 632.8 nm, which causes x_{eff} to become smaller, the maximum value measured of $-F_{12}(\theta)/F_{11}(\theta)$ increases a few percent for the majority of samples for which, at these two wavelengths, differences in $Im(m)$ are probably negligible. This effect is clearly strongest for the smallest particles, i.e., feldspar. However, the samples with the darkest colors, i.e., red clay and Lokon volcanic ash, that probably have the highest $Im(m)$, in particular for 441.6 nm, display a different wavelength dependence. It seems that for red clay the effect of a larger x_{eff} at 441.6 nm is nearly counterbalanced by a larger $Im(m)$ at this wavelength. For the Lokon sample, consisting of relatively large particles, the sizes are probably for a large part within the geometric optics domain, and the maximum value of $-F_{12}(\theta)/F_{11}(\theta)$ at 441.6 nm is considerably higher than that at 632.8 nm. This is probably due to a combined effect of a larger x_{eff} and a higher $Im(m)$ value at 441.6 nm.

The measured values of $F_{22}(\theta)/F_{11}(\theta)$ in Figures 5-11 decrease smoothly from close to unity in the forward direction to a minimum in the side-scattering range and then increase again toward backscattering angles. Often, $F_{22}(\theta)/F_{11}(\theta)$ is used as a measure of nonsphericity, because this ratio equals unity at all scattering angles for homogeneous optically nonactive spheres. However, for irregular samples, this ratio is affected not only by irregularity but also by particle size and complex refractive index. For instance, the Sahara sand sample, which contains the largest particles, exhibits the deepest minimum, and the feldspar sample, which contains the smallest particles, displays the shallowest minimum, as can be seen in Figure 12 (bottom panel). Furthermore, the $F_{22}(\theta)/F_{11}(\theta)$ curves of the dark-colored samples, red clay and Lokon volcanic ash, with probably the highest $Im(m)$, display an opposite wavelength dependence compared to the other samples (with the exception of Sahara sand for which the accuracy is very low).

Unlike for homogeneous optically nonactive spheres, $F_{44}(\theta)/F_{11}(\theta)$ and $F_{33}(\theta)/F_{11}(\theta)$ are substantially different for each sample (see Figures 5-11). Comparison of these two ratios shows that in most cases, $F_{33}(\theta)/F_{11}(\theta)$ is zero at a smaller scattering angle than $F_{44}(\theta)/F_{11}(\theta)$ and that $F_{33}(\theta)/F_{11}(\theta)$ exhibits in all cases a lower minimum than $F_{44}(\theta)/F_{11}(\theta)$. This behavior is also seen in many results of calculations, e.g., for spheroids, cylinders, and ellipsoids [Kuik, 1992; Mishchenko et al., 1996b] and may be a characteristic of nonspherical particles in general [Mishchenko et al., 2000b].

The wavelength dependence of $F_{44}(\theta)/F_{11}(\theta)$ is markedly different for differently colored samples. For the light-colored particles (i.e., feldspar, quartz, and Pinatubo ash) the results of the measurements at 441.6 nm are below those at 632.8 nm at small scattering angles. The curves cross more or less at side-scattering angles, while at backscattering angles, the curves are considerably higher at 441.6 nm than at 632.8 nm. For the yellow-brown particles (i.e., loess and Sahara sand) the higher $F_{44}(\theta)/F_{11}(\theta)$ curves at 632.8 nm deviate most from those at 441.6 nm around 45°, whereas they are close to each other at backscattering angles. For the red clay and the Lokon ash, the $F_{44}(\theta)/F_{11}(\theta)$ curve at 441.6 nm remains below the curve at 632.8 nm over the entire angle range. This different wavelength dependence is likely due to differences in the complex refractive indices of the samples.

The $F_{34}(\theta)/F_{11}(\theta)$ ratios show a large similarity for all aerosol samples investigated (see Figures 5-11). The ratios typically have a slight negative dip at small scattering angles and are positive at side-scattering angles, as is often found for nonspherical particles in general [Mishchenko et al., 2000b]. The maximum values measured at side-scattering angles range from 0.07 (loess, 441.6 nm) to 0.17 (quartz, 632.8 nm).

5.3. Average Aerosol-Scattering Matrix

The experimentally determined scattering matrix elements for the distinct samples are generally found to agree well in their overall trends and behavior. This is independent of the wavelengths considered. Therefore although detailed differences are present in the measured scattering matrices and it is preferable to take such differences into account in applications involving light scattering by mineral particles, we consider it justified to construct an average aerosol-scattering matrix for use, for example, in remote sensing studies for which the specific properties of the mineral aerosols are often not known.

The average aerosol-scattering matrix was obtained as follows: First, the average aerosol phase function, $F_{11}(\theta)$, was determined by averaging the 14 phase functions measured at both wavelengths. Since no scattering cross sections were available, the phase functions were averaged giving them equal weights. The 14 phase functions were all normalized to one at 30° (as shown in

Table 3. Average Aerosol Scattering Matrix Elements As Functions of the Scattering Angle[a]

Angle (deg)	F_{11}	$-F_{12}/F_{11}$	F_{22}/F_{11}	F_{33}/F_{11}	F_{34}/F_{11}	F_{44}/F_{11}
5	22.39	0.00	0.96	0.97	−0.01	0.96
10	7.37	0.01	0.94	0.96	−0.01	0.93
15	3.52	0.01	0.92	0.93	−0.02	0.88
20	2.08	0.00	0.89	0.89	−0.01	0.84
25	1.39	0.01	0.86	0.86	−0.00	0.80
30	1.00	0.01	0.84	0.82	0.00	0.74
35	0.75	0.02	0.80	0.79	0.01	0.71
40	0.59	0.02	0.77	0.74	0.02	0.66
45	0.47	0.03	0.74	0.69	0.03	0.62
50	0.39	0.05	0.70	0.64	0.04	0.56
55	0.33	0.06	0.68	0.61	0.05	0.53
60	0.28	0.07	0.63	0.54	0.06	0.48
65	0.25	0.08	0.60	0.49	0.07	0.44
70	0.22	0.10	0.56	0.41	0.08	0.39
75	0.20	0.10	0.52	0.36	0.10	0.35
80	0.18	0.11	0.50	0.30	0.10	0.31
85	0.17	0.11	0.45	0.24	0.10	0.27
90	0.16	0.12	0.43	0.18	0.11	0.23
95	0.15	0.12	0.41	0.12	0.10	0.19
100	0.14	0.12	0.38	0.06	0.10	0.17
105	0.14	0.12	0.36	0.02	0.10	0.12
110	0.13	0.12	0.34	−0.04	0.09	0.09
115	0.13	0.10	0.34	−0.09	0.07	0.06
120	0.13	0.09	0.31	−0.13	0.07	0.03
125	0.13	0.09	0.33	−0.15	0.08	0.00
130	0.13	0.06	0.31	−0.19	0.05	−0.02
135	0.12	0.06	0.32	−0.22	0.07	−0.04
140	0.12	0.05	0.31	−0.23	0.04	−0.07
145	0.13	0.03	0.32	−0.28	0.04	−0.09
150	0.13	0.02	0.35	−0.28	0.03	−0.09
155	0.13	0.01	0.35	−0.32	0.04	−0.15
160	0.13	0.00	0.36	−0.34	0.01	−0.15
165	0.13	−0.01	0.37	−0.34	−0.01	−0.17
170	0.14	−0.01	0.40	−0.35	0.01	−0.16
171	0.14	−0.01	0.41	−0.35	−0.02	−0.16
172	0.15	−0.02	0.40	−0.39	−0.01	−0.15
173	0.15	−0.00	0.42	−0.38	−0.01	−0.17

[a] $F_{11}(\theta)$ is normalized to one at $30°$.

Figures 5-11), and hence this normalization also holds for the average phase function, given in column 2 of Table 3. Second, each measured element ratio was multiplied with the normalized phase function that was measured for the particular sample and wavelength, thus yielding elements instead of element ratios. Third, for each pair of indices (i, j) the element $F_{ij}(\theta)$ of the average aerosol-scattering matrix was obtained by averaging the 14 corresponding elements. Finally, division by the average phase function yielded the element ratios of the average aerosol-scattering matrix shown in Table 3. The resulting average aerosol-scattering matrix obeys the Cloude test at each angle tabulated.

The average aerosol-scattering matrix is displayed in Figure 13 by means of squares. For comparison, we also indicate in Figure 13 the domain covered by the best values of all measurements, i.e., the area between the highest and lowest measured values in Figures 5-11 not taking into account the error bars for the individual

measurements. In section 6 we will compare this matrix and the domain occupied by the samples with results of ray-optics calculations.

6. Model Calculations

In section 6.1 we give a description of the light scattering model used to analyze the measured values of the scattering matrix elements. A sensitivity study for this model is presented in section 6.2. We compare the results of the calculations with the average aerosol-scattering matrix in section 6.3 and with the individual measurements in section 6.4.

6.1. Ray-Optics Method

To compute the light-scattering behavior of an ensemble of randomly oriented mineral aerosols, a method is required that takes into account in detail the high irregularity and large variety in size and shape of mineral
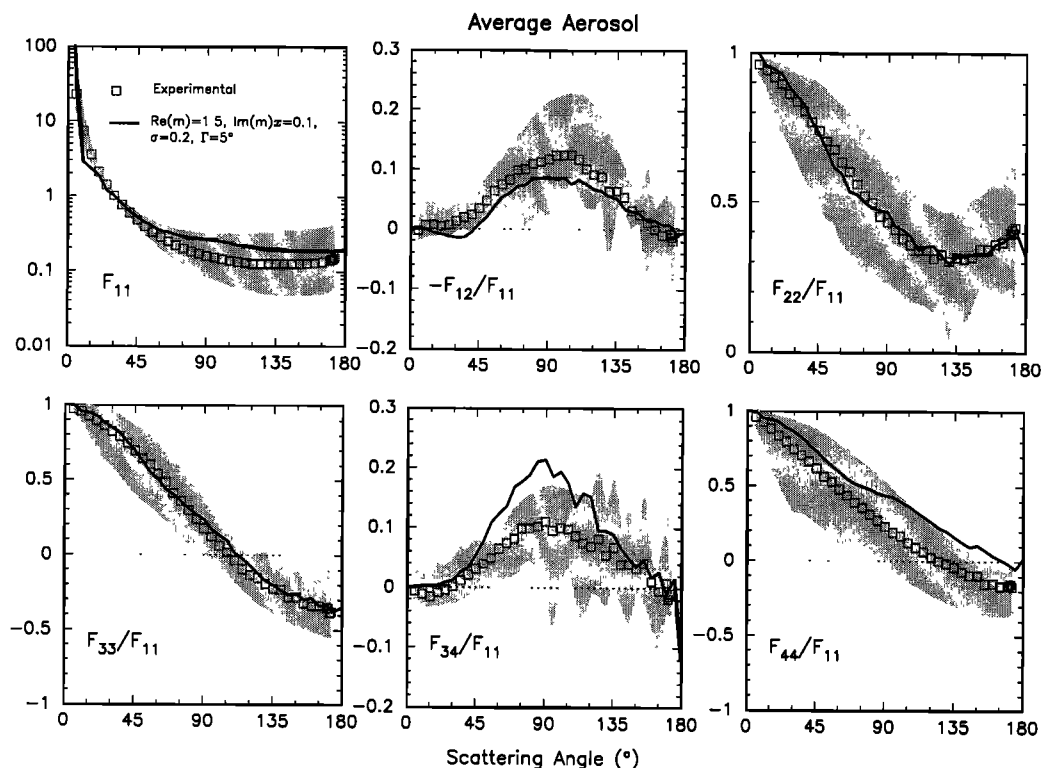
Figure 13. Average aerosol scattering matrix element $F_{11}(\theta)$, and element ratios $-F_{12}(\theta)/F_{11}(\theta)$, $F_{22}(\theta)/F_{11}(\theta)$, $F_{33}(\theta)/F_{11}(\theta)$, $F_{34}(\theta)/F_{11}(\theta)$, and $F_{44}(\theta)/F_{11}(\theta)$ (squares). The domains occupied by the measurements presented here are indicated in grey. Solid lines in the plots are the results of ray-optics calculations for Gaussian random particles with $x_{eff}=47$, $\Gamma=5°$, and $\sigma = 0.2$ (see section 6).

aerosols. Here we will use the ray-optics approximation [*Muinonen et al.*, 1996; *Muinonen*, 2000], because this method is able to deal with complex aerosol shapes.

The range in size parameters x and refractive indices m for which the ray-optics approximation provides accurate results, i.e., $x \gg 1$ and $2x|m - 1| \gg 1$, is not well defined, since it depends not only on the shape of the particles and on $\mathrm{Im}(m)$ but also on the type of scattering properties to be calculated [*Macke et al.*, 1995; *Mishchenko et al.*, 2000b]. Macke et al. compared exact T-matrix results for F_{11} and $-F_{12}/F_{11}$ for randomly oriented spheroids with an axis ratio of 2 with ray-optics results and found that ray optics is more accurate for spheroids than for spheres. Ray optics gives reasonably accurate phase functions for spheroids with surface-equivalent size parameters $x > 60$, while for spheres, x has to be of the order of a few hundreds. Increasing sample irregularity and absorption will tend to make ray-optics calculations even more accurate and applicable to smaller particles, since in these cases interference effects of different rays leaving the particles, which are not taken into account in ray optics, become less important [see also *Peltoniemi et al.*, 1989]. In short, for the samples containing the largest particles, the ray-optics approximation is expected to be useful, but the lower limit for x is unknown. For this reason, and because the scattering matrix elements as functions of the scat-

tering angle of all samples show such a remarkable degree of similarity, it is interesting to compare ray-optics results with all experimental results, to investigate to which extent ray-optics results may yield an adequate description of the scattering behavior of our samples.

In the ray-optics approximation the total amount of light scattered by a particle is the sum of diffracted, reflected, and transmitted components [e.g., *Bohren and Huffman*, 1983, section 7]. In our calculations we combined a forward diffraction part and a geometric-optics part (taking into account reflected and transmitted rays) in a manner described by *Muinonen et al.* [1996]. In the diffraction part of the method, the refractive index of the particles does not occur and the forward diffraction peak is computed using a size distribution for equal-projected-surface-area spheres. In this way, the forward peak is assumed to be independent of the detailed shape of the particles [e.g., *Bohren and Huffman*, 1983, chapter 4]. In the geometric-optics part, in contrast, the size, shape, and refractive index of the aerosols are accounted for in detail. In this case, a model particle in a specific orientation is newly generated for each incident ray, which comes from a random direction. At each boundary surface, reflection and refraction take place according to Snell's law, and to Fresnel's reflection and refraction matrices [*Muinonen et al.*, 1996; *Muinonen*, 2000]. This procedure is repeated for

many rays to obtain an ensemble average over many particles and orientations.

The model particle is generated according to a statistical method based on Gaussian random shapes (shape distributions) as described extensively by *Muinonen et al.* [1996] and *Muinonen* [2000]. In principle, there are many different ways to parameterize a Gaussian random shape. In our method, Gaussian random shapes are functions that describe spherical shapes with random surface deformations. We confine ourselves to a relatively simple parameterization for which results of calculations have been published by *Muinonen et al.* [1996]. Using this parameterization, a Gaussian random shape is described by the relative standard deviation σ of the radius vector of the deformed sphere and the correlation angle Γ of the surface deformations. The correlation angle Γ determines the number of hills and valley deformations per solid angle and can take values in the range $0° < \Gamma \leq 180°$, where a relatively small value corresponds to a high number of peaked surface deformations. Increasing σ enhances the heights of the hills and the depths of the valleys radially.
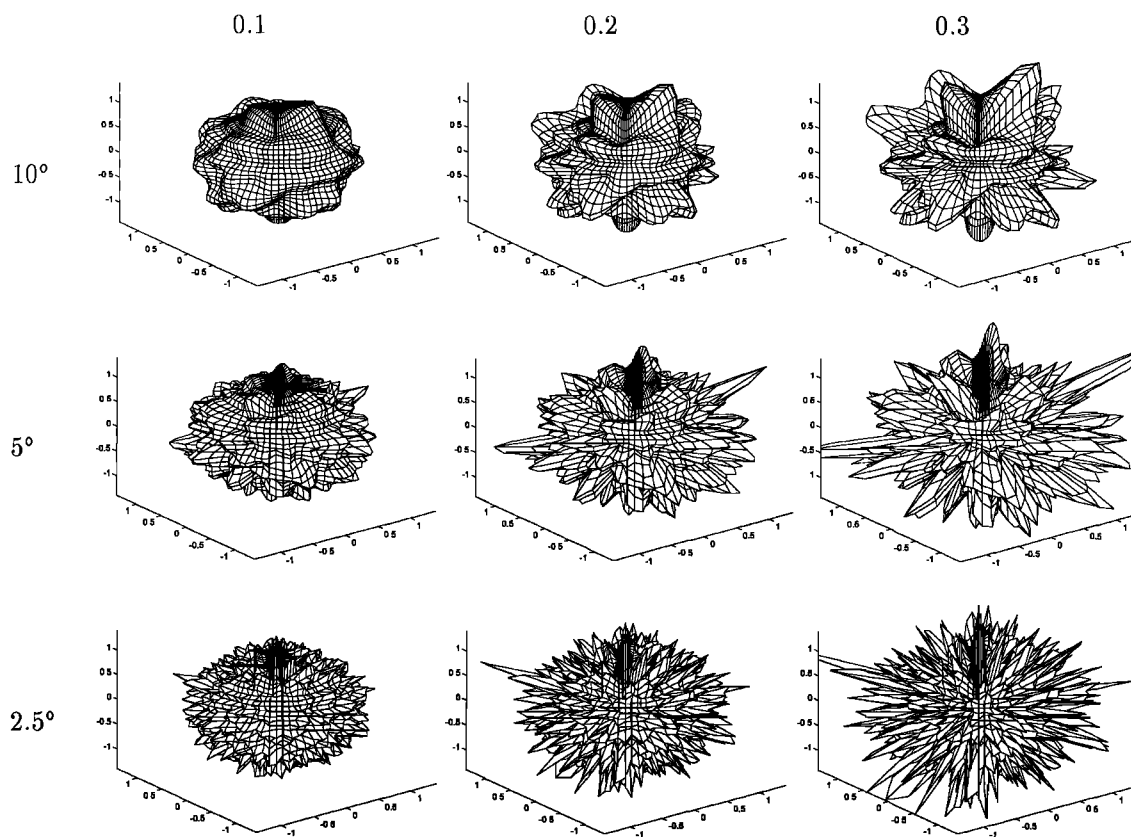
With a given Gaussian random shape, many different Gaussian random particles can be created. Some visualizations of typical examples of Gaussian random particles (i.e., model particles used in the computational method) are shown in Figure 14.

If no absorption occurs, the size of the particles does not influence the geometric-optics calculations. Therefore the average radius vector of the Gaussian random particles is chosen to be unity. In case absorption does occur, the size of the particles is accounted for in the product $\text{Im}(m)x$

We emphasize that since we employ a statistical method to calculate the scattering matrices, the shapes of the individual particles in the aerosol samples studied (see Figure 2) need not and, in fact, do not resemble those of the individual model particles. The main differences are that the aerosol particles in the samples vary strongly in size, have inhomogeneities, and have no spikes. However, although there is no one-to-one correspondence between the aerosol particles and the Gaussian random particles, the light scattering properties of an ensemble of Gaussian random particles in the geometric-optics approximation are expected to be representative for large aerosol particles. We note the following examples [see also *Muinonen*, 2000]:

1. In the geometric-optics calculations, a ray coming from a random direction may encounter a peaked surface deformation without being affected by the rest of

Figure 14. Visualizations of typical examples of Gaussian random particles. These particles were generated using Gaussian random shapes with a relative standard deviation of the radius vector $\sigma=0.1$, 0.2, and 0.3 (columns, left to right), and correlation angles $\Gamma=10°$, $5°$, and $2.5°$ (rows, top to bottom).

the Gaussian random particle.From a light scattering point of view, this is similar to a ray that encounters an aerosol particle that is relatively small in size.

2. Similarly, a ray incident in the direction of a peaked surface deformation may travel through the entire Gaussian particle. From a light-scattering point of view, this is similar to a ray encountering a relatively large aerosol particle.

The probability for these extreme ray-particle interactions to occur is higher for Gaussian random particles with more peaks and/or more extended peaks, i.e., for smaller values of Γ and/or larger values of σ. Consequently, light scattering by an ensemble of Gaussian random particles for a small value of Γ and/or large value of σ is similar to light scattering by an ensemble of aerosol particles with a broad projected-surface-area distribution. (Note that the σ of the Gaussian random particles cannot be compared directly with the σ_{eff} obtained for the mineral aerosols, although they would denote similar quantities in case the Gaussian random particles would be perfectly spherical.)

In the same manner, a ray incident on a Gaussian random particle with a relatively larger number of highly peaked surface deformations, i.e., a smaller value of the correlation angle Γ, and a larger value of σ, probably will experience much interaction with the particle, encountering many boundary surfaces. Therefore an ensemble of such Gaussian random particles will exhibit light-scattering behavior similar to that of an ensemble of aerosol particles with a high degree of internal and/or external irregularity.

In conclusion, we expect that the ray-optics method, by means of its statistical approach, takes into account adequately effects of the high irregularity on the light-scattering behavior of large aerosol particles.

6.2. Outline of the Model Computations

In this section we briefly describe how the ray-optics method is applied to investigate the measured scattering matrices of the aerosol samples presented in section 5.

The geometric-optics part of the ray-optics method to calculate the scattering matrix of the Gaussian random particles depends on the statistical parameters σ and Γ, on the real part of the refractive index $Re(m)$, and on the imaginary part of the refractive index times the size parameter $Im(m)x$ [see *Muinonen et al.,* 1996]. As discussed in section 6.1, the diffraction part is calculated separately. This part is added to the geometric-optics part to obtain the complete ray-optics scattering matrix as a function of scattering angle.

We investigated the sensitivity of the scattering matrices of ensembles of Gaussian random particles by
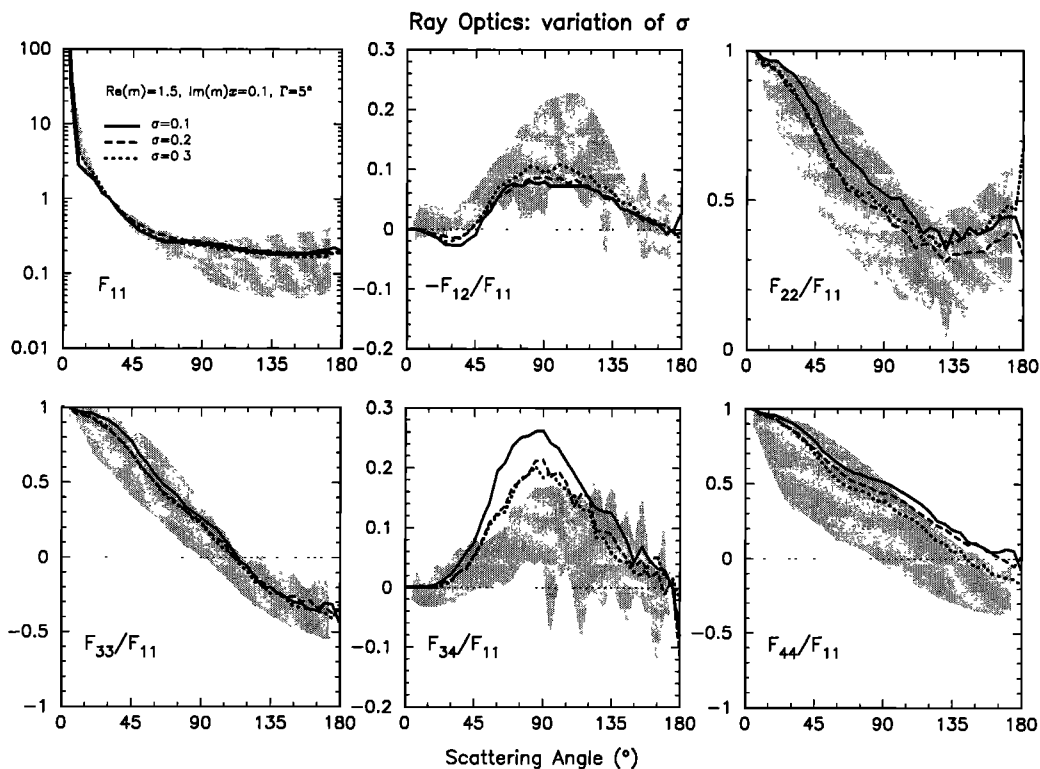
Figure 15. Scattering matrix elements computed with the ray-optics method. The standard deviation σ of the radius vector is varied from 0.1 (solid line), to 0.2 (dashed), and 0.3 (dotted). Further, we used $x = 47$, $Re(m) = 1.5$, $Im(m)x = 0.1$, and $\Gamma = 5°$. Shaded areas indicate the domain covered by the results of the measurements.
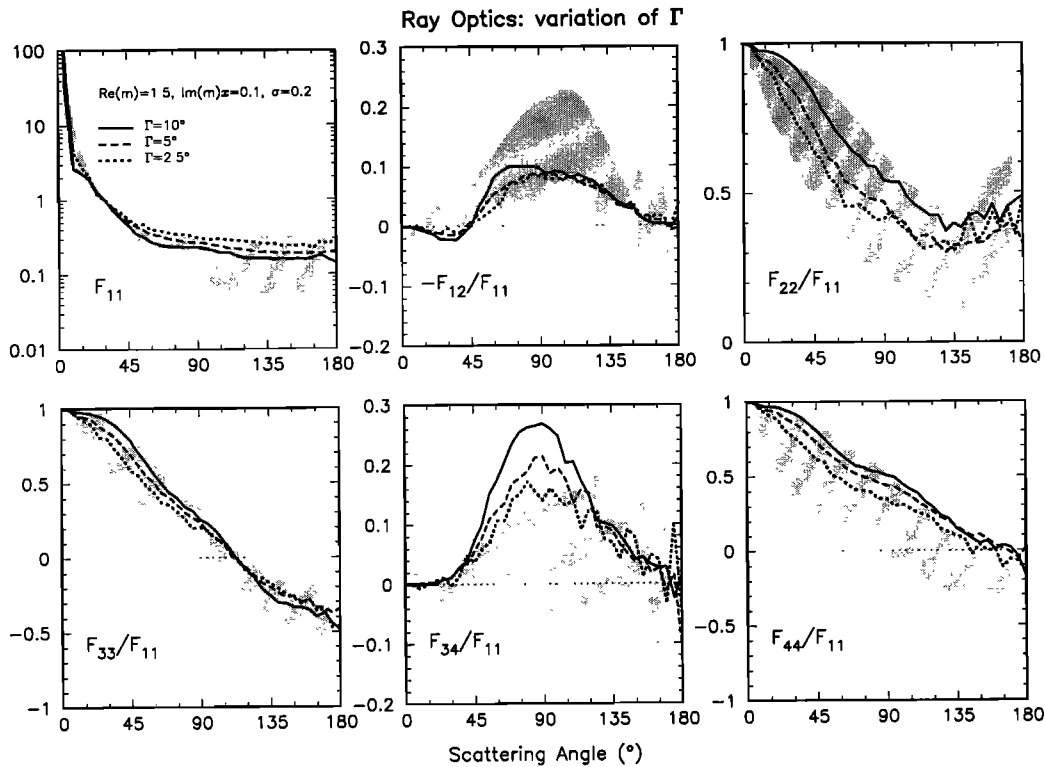
Figure 16. Same as Figure 15 but for variations in the correlation angle Γ from $10°$ (solid line), to $5°$ (dashed), and $2.5°$ (dotted). Further, we used $x = 47$, $Re(m) = 1.5$, $Im(m)x = 0.1$, and $\sigma = 0.2$.

systematically varying σ and Γ, $Re(m)$, and $Im(m)x$. To the geometric-optics results we added a forward peak (as described by Muinonen, [2000]), calculated for equal-projected-area spheres (corresponding to the Gaussian random particles used) with a size parameter $x=47$, i.e., the mean value of x_{eff} for all samples at two wavelengths. We use this average peak for the sensitivity study, because differences in the diffraction peak hardly influence the shape of the resulting scattering matrix elements as functions of the scattering angle.

For the geometric-optics calculations we have chosen the following parameter values, appropriate for the aerosol samples studied (see also Table 1): $\sigma = 0.1, 0.2$, 0.3, $\Gamma = 2.5°, 5°, 10°$, $Re(m) = 1.3\text{-}1.8$ (in steps of 0.1), and $Im(m)x = 0.004, 0.04, 0.1, 0.2, 0.3, 0.4$. $Im(m)x < 0.004$ gives results similar to those for $Im(m)x=0.004$. Increasing $Im(m)x$ beyond 0.4 produces results that are outside the domain covered by the measurements considered in this paper.

For each combination of parameter values calculated, we secured sufficient accuracy by using 50.000 Gaussian particles and corresponding random incident rays. Nevertheless, some statistical noise remains in the resulting matrix elements. In particular, at backward scattering angles the noise is apparently appreciable, as can be seen from the violations of the general equalities [Mishchenko and Hovenier, 1995; Hovenier and van der Mee, 2000]

$$F_{12}(180°)/F_{11}(180°) = F_{34}(180°)/F_{11}(180°) = 0, \quad (7)$$

$$F_{22}(180°)/F_{11}(180°) = -F_{33}(180°)/F_{11}(180°), \quad (8)$$

$$F_{44}(180°)/F_{11}(180°) = 1 - 2F_{22}(180°)/F_{11}(180°). \quad (9)$$

This large noise is due to the fact that few rays are scattered in backward directions; the amount of forward scattering relative to backward scattering can easily differ a factor of 10^4. The computations for the complete scattering matrices as functions of the scattering angle lasted from a few hours to several weeks on a work station (IBM RS6000/604 PowerPC) for one set of parameter values. Increasing the number of rays and generated particles, as well as decreasing Γ or increasing σ, will result in longer computing times. We verified that the results of the calculations obey the Cloude test.

6.3. Results of Calculations Compared With the Average Scattering Matrix

In Figures 15-18 we present the computed scattering matrices as functions of the scattering angle for various combinations of σ, Γ, $Re(m)$, and $Im(m)x$. As a reference model, we adopt the central values of the parameter range employed, i.e., $\sigma=0.2$, $\Gamma=5°$, $Re(m)=1.5$, $Im(m)x=0.1$, and $x=47$. When considering the variation of one parameter in Figures 15-18, the values of remaining parameters correspond to the reference model. Furthermore, we use a resolution of $5°$ for the angu-

Ray Optics: variation of Re(m)
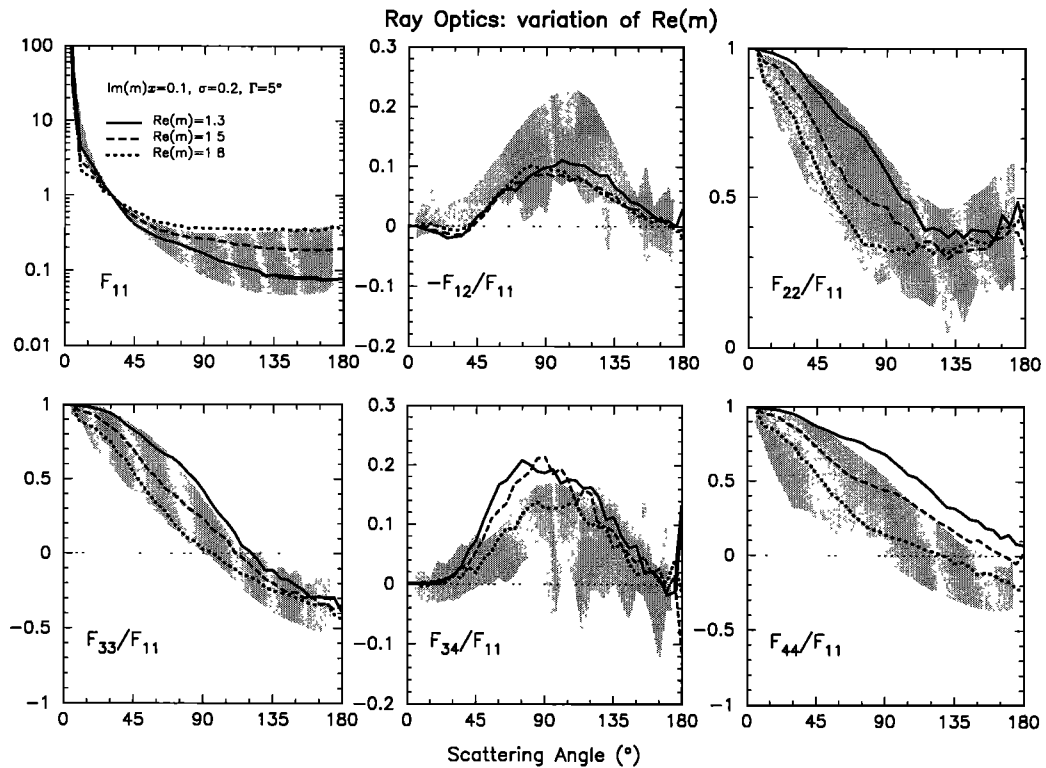
Figure 17. Same as Figure 15 but for variations in $Re(m)$ from 1.3 (solid line), to 1.5 (dashed), and 1.8 (dotted). Further, we used $x = 47$, $Im(m)x = 0.1$, $\Gamma = 5°$, and $\sigma = 0.2$.

Ray Optics: variation of Im(m)x
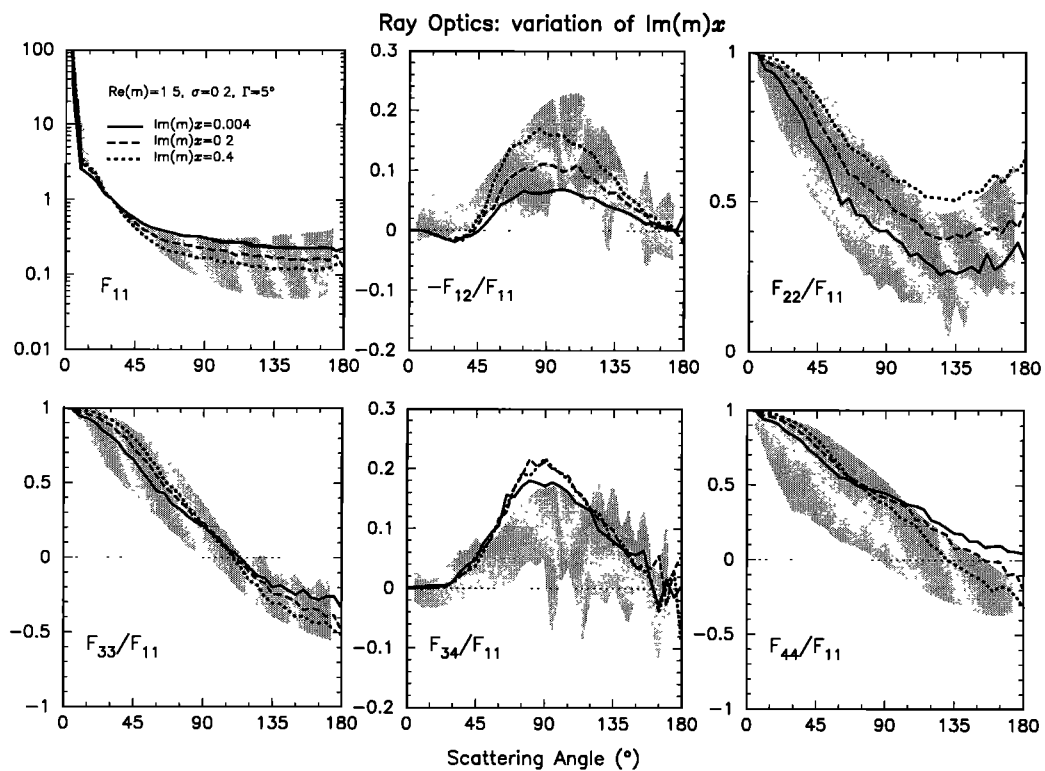
Figure 18. Same as Figure 15 but for variations in $Im(m)x$ from 0.004 (solid line), to 0.2 (dashed), and 0.4 (dotted). Further, we used $x = 47$, $Re(m) = 1.5$, $\Gamma = 5°$, and $\sigma = 0.2$.

lar bins corresponding to the angular resolution of the measurements for $\theta < 170°$.

The effects of varying σ on the computed scattering matrix elements are presented in Figure 15. For all scattering matrix computations shown we find good overall agreement with the aerosol measurement domain as mentioned in section 5.3, except for the element ratio $F_{34}(\theta)/F_{11}(\theta)$. The effect of varying σ is substantial for $F_{22}(\theta)/F_{11}(\theta)$, $F_{34}(\theta)/F_{11}(\theta)$, and $F_{44}(\theta)/F_{11}(\theta)$ and small for $F_{11}(\theta)$, $-F_{12}(\theta)/F_{11}(\theta)$, and $F_{33}(\theta)/F_{11}(\theta)$. Overall, we find that increasing σ reduces the differences between the results of the measurements and those of the calculations. The model results suggest that values of $\sigma > 0.3$ would improve the agreement with the measurements for, for example, $F_{44}(\theta)/F_{11}(\theta)$. However, such improvements will be limited since values of $\sigma > 0.3$ produce ray-optics results very similar to those for $\sigma = 0.3$ (see further *Muinonen et al.* [1996]).

The effects on the model results of varying Γ are shown in Figure 16. In general, good overall agreement with the measurements is found, except for $F_{34}(\theta)/F_{11}(\theta)$ if $\Gamma > 2.5°$. Note that as is the case for σ, varying Γ hardly affects $-F_{12}(\theta)/F_{11}(\theta)$ but changes several other elements considerably, most notably $F_{22}(\theta)/F_{11}(\theta)$. Interestingly, varying Γ from $10°$ to $2.5°$ has a largely similar effect on the ray-optics results as varying σ from 0.1 to 0.3. This might be due to the fact that both parameters influence the degree of irregularity of the ensemble particles.

The results of varying $Re(m)$ for the computed scattering matrix elements are shown in Figure 17. We find that when $Re(m)$ is varied from 1.3 to 1.8, this has a relatively strong effect on $F_{11}(\theta)$ and all matrix element ratios except $-F_{12}(\theta)/F_{11}(\theta)$. In particular, the steepness of $F_{11}(\theta)$ strongly decreases with increasing values of $Re(m)$. This can be explained by the fact that a higher value of $Re(m)$ causes a larger fraction of the incident light to be reflected. At the same time, the $F_{22}(\theta)/F_{11}(\theta)$, $F_{33}(\theta)/F_{11}(\theta)$, $F_{34}(\theta)/F_{11}(\theta)$, and $F_{44}(\theta)/F_{11}(\theta)$ ratios decrease when $Re(m)$ increases, especially at side-scattering angles.

The effects of varying $Im(m)x$ are shown in Figure 18. The steepness and shape of $F_{11}(\theta)$ is affected by $Im(m)x$ but in a manner different from that caused by variations in $Re(m)$. It appears that $Im(m)x$ is the only parameter that modifies $-F_{12}(\theta)/F_{11}(\theta)$ substantially. At side-scattering angles, $-F_{12}(\theta)/F_{11}(\theta)$ increases with increasing values of $Im(m)x$ (compare section 5.2).

Overall, the results of the ray-optics calculations are well within the domain occupied by the measurements and can adequately describe the main part of the differences found among the measured results for the irregular mineral particles studied here. The only notable exception to this is $F_{34}(\theta)/F_{11}(\theta)$. To improve the results for this ratio without affecting the results for the other element ratios, it is probably necessary to increase the irregularity of the model particles, e.g., by consider-

ing simultaneously smaller values of Γ and larger values of σ. However, we have refrained from doing this, since computing times become very large for such parameter values, while $F_{34}(\theta)/F_{11}(\theta)$ is usually of relatively less importance, e.g., for (single or multiple) scattering in the Earth's atmosphere.

6.4. Comparison With Results of Individual Samples

In addition to the overall comparison of the ray-optics calculations with the measurements, we investigated in more detail whether the results of the computations can reproduce the behavior of the scattering matrix elements of the individual aerosol samples both at 632.8 nm and at 441.6 nm. To be able to perform ray-optics calculations for our samples individually, we needed to choose values for the parameters σ, Γ, x, $Re(m)$, and $Im(m)x$. As in section 6.3, we fixed the parameters $\sigma = 0.2$ and $\Gamma = 5°$. For the diffraction peak calculations, we used $x = x_{eff}$ for each combination of sample and wavelength individually. We chose the parameters pertaining to the refractive indices from the range of values provided by the literature (see Table 1). Since these literature values usually allowed for a narrow range of acceptable values, a final choice within the range was made by attempting to reproduce (qualitatively) the various wavelength dependences of $F_{22}(\theta)/F_{11}(\theta)$, $F_{33}(\theta)/F_{11}(\theta)$, and $F_{44}(\theta)/F_{11}(\theta)$ measured for our samples. We adopted this method since for the wavelength dependences of these ratios the effects of differences in $Re(m)$ and $Im(m)x$ are markedly different (see Figures 17 and 18), so we can fit these parameters independently. We emphasize that in this study we aimed at reproducing scattering matrices as functions of the scattering angle and not at deriving aerosol properties.

The final ray-optics results are shown in Figures 5-11 and Figure 13 together with the measured results. The parameters $Re(m)$ and $Im(m)x$ used for the specific aerosol samples at 632.8 nm or 441.6 nm are indicated in the legends of the corresponding figures.

We obtained a satisfactory overall resemblance between measured and calculated results for all aerosol samples studied. As expected, the resemblance is better for the larger particles, such as Lokon volcanic ash, but a remarkably good agreement is also found, for example, for the much smaller quartz particles. Since all of our samples contain a considerable fraction of small particles, all results may be influenced to different degrees by their presence. In general, their influence seems to manifest itself most clearly in $F_{11}(\theta)$ and $-F_{12}(\theta)/F_{11}(\theta)$. This can be seen for instance from the increasingly too low steepness of the calculated $F_{11}(\theta)$ for decreasing x_{eff}. Also, the calculated $-F_{12}(\theta)/F_{11}(\theta)$ tends to show a too low maximum for decreasing x_{eff} (compare section 5.2). In particular, we can conclude from the comparison between these measured and cal-

culated elements that the feldspar particles and red clay particles are too small to obtain accurate results from ray-optics calculations, even though their general behavior is still similar to the ray-optics results. For these samples, we encountered the additional problem that for the diagonal element ratios the diffraction part of the calculations starts to contribute at large scattering angles, which impedes drawing further conclusions for these samples.

The best agreement between calculated results and measured results is found for the element ratios $F_{22}(\theta)/F_{11}(\theta)$ and $F_{33}(\theta)/F_{11}(\theta)$. More difficult to reproduce seem to be the element ratios $F_{34}(\theta)/F_{11}(\theta)$ and $F_{44}(\theta)/F_{11}(\theta)$, especially for the brown-colored samples such as Sahara sand, Lokon volcanic ash, and loess. They tend to be above the measured results for most of the scattering angle range.

The observed differences between measurements conducted at different wavelengths can be reproduced at least qualitatively by choosing appropriate values from the range of literature values for the parameters $Re(m)$ and $Im(m)x$. This ability to reproduce the wavelength dependence provides valuable information about the influence of the complex refractive index and size parameter on the measurements as well as the computations. For instance, the ray-optics results shown in Figures 5-11 indicate a wavelength dependence in $Re(m)$ for the brown-colored samples loess, Lokon volcanic ash, and Sahara sand, which is expected for samples that contain a significant amount of iron (see section 2.2). It is consistent with such a higher iron content that the $Re(m)$ values for these samples appear to be smaller at 632.8 nm than at 441.6 nm. For the light-colored samples quartz and Pinatubo volcanic ash, $Re(m)$ appears to be the same at both wavelengths.

We have to be careful with our interpretation of the wavelength dependence found for the parameter $Im(m)x$ (see section 5.2). For the light-colored samples quartz and Pinatubo volcanic ash, we expect that $Im(m)$ is more or less the same at both wavelengths, while for the samples loess and Sahara sand the yellow brown color suggests a slightly larger $Im(m)$ value at 441.6 nm than at 632.8 nm. In both cases the parameter $Im(m)x$ should be smaller at 632.8 nm than at 441.6 nm. However, this is not what we found for the calculated results for these samples. This again indicates that part of the particles determining the behavior of $-F_{12}(\theta)/F_{11}(\theta)$ are too small to obtain accurate results from ray-optics calculations (see section 5.2). Another behavior is observed, e.g., for the dark brown Lokon ash, where $-F_{12}(\theta)/F_{11}(\theta)$ is larger at 441.6 nm than at 632.8 nm. Here we found from the ray-optics results that $Im(m)$ is apparently larger at 441.6 nm than at 632.8 nm, as is expected (see section 2.2).

For the individual ray-optics calculations the estimates of $Im(m)$ mostly lie in the range between 10^{-2} and 10^{-4}. This is within the range expected for natural particles [*Egan and Hilgeman*, 1979; *Gerber and*

Hindman, 1982]. However, we note that the $Im(m)$ values chosen tend to be higher for samples with smaller x_{eff}. Most likely, this reflects a tendency to reproduce the scattering properties of small particles by increasing the amount of absorption for the ray-optics calculations, since this has a similar effect, in particular, on the element ratio $-F_{12}(\theta)/F_{11}(\theta)$.

The calculated results corresponding to the reference model are shown in Figure 13 together with the measured average aerosol-scattering matrix. The comparison between the two results illustrates some general properties of the comparison for the individual samples. The parameter values used for the reference model calculations are $Re(m)=1.5$ and $Im(m)x=0.1$. The latter corresponds to $Im(m) \sim 10^{-3}$ taking $x = 47$ (see section 6.2). The average scattering behavior can be explained well by the ray-optics results for the reference model. For example, the steepness of $F_{11}(\theta)$ is reproduced very well, while for $F_{22}(\theta)/F_{11}(\theta)$ and $F_{33}(\theta)/F_{11}(\theta)$, the agreement is excellent for most scattering angles. At the same time, a number of more specific characteristics of the average aerosol matrix cannot be described in full detail. The largest discrepancies are found for $F_{34}(\theta)/F_{11}(\theta)$ and $F_{44}(\theta)/F_{11}(\theta)$. We argue that better agreement can be achieved for those element ratios by decreasing Γ and increasing σ (see Figures 15 and 16). This may also reduce the probably artificial knee in $F_{11}(\theta)$ near forward scattering angles which is often present (see Figure 15) in the domain where diffraction and ray-optics contributions meet. Furthermore, we note that the slight upturn at backscattering angles in the measured results of $F_{11}(\theta)$ as well as the negative dip in $-F_{12}(\theta)/F_{11}(\theta)$ at backscattering angles are not clearly reproduced in the results of the ray-optics calculations (see section 7.3 for a further discussion of this negative dip).

In summary, we find good overall agreement between the ray-optics results for scattering matrices of Gaussian random particles and the results of measurements of the irregular mineral aerosol samples characterized in section 2. In particular, the ray-optics calculations are able to reproduce qualitatively general trends observed in the wavelength dependence of the aerosol measurements. This indicates that these ray-optics calculations are useful for irregular samples, even when they have projected-surface-area distributions with a large fraction of very small particles.

7. Discussion

In section 7.1 we discuss in more detail the measurement results of the aerosol samples investigated in this paper. The comparison of these data with ray-optics results for Gaussian random shapes is discussed in section 7.2. Possible implications for scientific fields, such as studies of the Earth atmosphere by remote sensing and the light-scattering properties of planets and inter-

planetary bodies in the solar system, are discussed in section 7.3.

7.1. Aerosol Measurements

The results of the scattering matrix measurements presented in section 5 show a remarkable similarity in the general light-scattering behavior of the aerosol samples investigated. This is probably due to the irregularity of the aerosol samples. This finding is supported by several other measured scattering matrices or matrix elements of similar irregular mineral aerosol samples reported in the literature [see *Holland and Gagne*, 1970; *Jaggard et al.*, 1981; *Nakajima et al.*, 1989; *Kuik et al.*, 1991; *Kuik*, 1992; *West et al.*, 1997]; that is, the phase function $F_{11}(\theta)$ has a steep forward peak, virtually no structure at side-scattering and backscattering angles and no halo or rainbow features, while the $-F_{12}(\theta)/F_{11}(\theta)$ function has a bell shape with a maximum at side-scattering angles. The other element ratios show a behavior which in most cases fit into the domain covered by our measurements. It is interesting to note that the scattering matrix for ice crystals, as measured by *Dugin and Mirumyants* [1976], shows a strong resemblance to our results for mineral particles too. This suggests that their samples of ice crystals are sufficiently irregular to exhibit the same type of scattering behavior. *Perry et al.* [1978] found a similar scattering behavior for cubic (NaCl) crystals.

We argue that most irregular silicate aerosol samples have scattering matrices as functions of the scattering angle, which are very similar. In particular, we suggest that in the case of a sample of irregular aerosols with unknown scattering properties but with diameters roughly between 0.1 and 100 μm and $Re(m) \sim 1.5$, the scattering matrix can be described approximately by the average aerosol scattering matrix presented in section 5. This average scattering matrix can be used, for example, as input in remote sensing studies or to verify the applicability of assumptions made in light-scattering calculations. For instance, *Braak et al.* [2001] used this and other measured matrices in a study of parameterized scattering matrices to choose a particular parameterization. Such parameterized scattering matrices can be used in analyses of polarization measurements of planets where reliable a priori assumptions on particle shapes or sizes cannot be made.

Within this common type of scattering behavior, detailed scattering characteristics are found to be determined by properties such as the size distribution [cf. *Nakajima et al.*, 1989; *Kuik*, 1992] and composition of the aerosols. In particular, the differences in wavelength dependence observed for the individual samples may be a useful tool to distinguish between different types of irregular aerosols. For instance, one may select the most sensitive matrix element and scattering angle to monitor a specific aerosol characteristic (e.g., in situ or with lidar instruments) with the help of the extensive data set presented here.

7.2. Model Calculations

We have used the average scattering matrix and the scattering matrices of the individual samples to investigate whether the ray-optics approach in conjunction with Gaussian random shapes gives insight in the mechanisms that determine the light-scattering behavior we measured for our aerosol samples. In most cases, we were able to find good agreement between the measured results and the calculated results for our aerosol samples by varying the refractive index and a few model parameters specifying the shape of Gaussian particles, even for the samples containing a large fraction of very small particles. To our knowledge, such agreement between computations and measurements for irregular mineral particles has not been accomplished yet by any other numerical approach for all the matrix elements as functions of the scattering angle.

We analyzed our measured results by varying the refractive index within the range allowed by the literature values, in order to reproduce the wavelength dependence of the matrix element ratios. We have been able to find ray-optics results with the same qualitative behavior as the measured results at the two visual wavelengths at which the measurements were performed for nearly all phase functions and matrix element ratios. We compare values of the parameters $Re(m)$ and $Im(m)x$ that correspond to these fits with the values reported in the literature as follows:

1. From the comparison between measured and calculated results for loess, Sahara sand, and Lokon volcanic ash, we find indications for a wavelength dependence. For these samples, $Re(m)$ appears to be larger at 441.6 nm than at 632.8 nm. Since these samples have a brown color, we propose that iron oxides are responsible for this behavior, because iron oxides, even when present in small amounts, produce a strong wavelength dependence both for $Re(m)$ and $Im(m)$ (see section 2.2) [e.g., *Egan and Hilgeman*, 1979].

2. Values for $Im(m)$, derived from $Im(m)x$ using the corresponding values for x_{eff} for each measurement, lie largely in the range $Im(m) = 10^{-2} - 10^{-4}$, which is in agreement with values for natural particles [*Egan and Hilgeman*, 1979; *Gerber and Hindman*, 1982]. However, for light-colored samples like quartz, a lower value of $Im(m)$, i.e., of the order of 10^{-5}, was expected based on literature values [e.g., *Klein and Hurlbut*, 1993]. The reason for the larger values may be that the value for this parameter $Im(m)$ for the ray-optics calculations is sometimes chosen too high, for example, to increase the height of the maximum of $-F_{12}(\theta)/F_{11}(\theta)$, while this high maximum in the measurements is instead due to the presence of many small particles rather than to a high $Im(m)$ (see section 6.4). An alternative explanation is that $Im(m)$ is extremely sensitive to mineral composition. Therefore a difference of an order of magnitude from values found in the literature is quite common.

Regarding the parameterization of particle irregularity by means of a Gaussian random shape, as described by the parameters σ and Γ, we note that the agreement between the measurements and the ray-optics calculations may be slightly improved for some aerosol samples, if values of $\sigma > 0.3$ and values for $\Gamma < 2.5°$ are taken into account. However, a great number of calculations performed for these values would require faster computers. The reason that such extreme values for σ and Γ are required to improve the comparison for individual aerosol samples may be that the present model does not account for internal inhomogeneities and small-scale structures on the surface of the aerosols (see Figure 2h). A more advanced parameterization of Gaussian random shapes [see Muinonen, 2000] may improve the comparisons but would eventually require a detailed shape analysis of the aerosol samples. Such a shape analysis may have to be performed on several thousands of particles to account for the large diversity in shape and size of the particles in the sample. Clearly, this is a complex and time-consuming task, while internal structures still would not be accounted for.

Aerosol samples consisting of very small particles, such as feldspar and red clay, are too small to be described accurately by ray optics (see Figure 5) [see also Macke et al., 1995]. For future research, it is interesting to compare the measured matrix elements of such aerosol samples with T-matrix results for spheroids. This method is suitable for micron-size particles in the visible and has produced promising results [Jaggard et al., 1981; Mishchenko et al., 1997]. In this method, the irregularity of the aerosol particles is accounted for by employing a size-shape mixture of spheroids. If a sufficiently broad shape distribution is included, the phase function can be reproduced well [see also Hill et al., 1984]. However, in general, the calculated phase function may become rather shallow by incorporating too high values of Im(m). Jaggard et al. [1981] and Nakajima et al. [1989] found this for Mie calculations, while Vermeulen [1999] found this effect in a comparison between measured scattering matrix elements and T-matrix results for a probably too narrow shape-size distribution of spheroids. The danger of unknowingly incorporating too high values of Im(m) to obtain a good fit for the phase function can be avoided by employing the angular dependence of the other scattering matrix elements, since these elements give more constraints to the fits and are often more sensitive to parameters such as Im(m). Therefore we emphasize that it is important to investigate the scattering matrix as a whole, as we did in the present paper.

7.3. Importance for Earth's Sciences and Astronomical Topics

Although several observations are made to determine properties of irregular mineral particles in the Earth's atmosphere, and the importance of these particles has been recognized by many authors [e.g., Herman et al.,

1997; Kaufman et al., 1997; Mishchenko et al., 1997], the interpretation of such observations is hampered by the lack of knowledge on the light-scattering properties of these particles. The extended set of experimental results for the relatively well characterized aerosols presented in this paper may, at least partly, solve these problems and may help to interpret (or classify) satellite observations in terms of aerosol properties, such as irregularity, size, and refractive index [e.g., Herman et al., 1997].

Irregular mineral particles also occur abundantly in objects of astronomical interest. Proof of this are the many irregularly shaped silicate particles of extraterrestrial origin collected in the stratosphere [Warren et al., 1997] and spectral data of circumstellar dust shells containing crystalline silicates [e.g., Molster et al., 1999]. In fact, Weiss-Wrana [1983] argued that there are no principal differences between the scattering characteristics of cosmic and terrestrial mineral particles. She compared the results of laboratory measurements of $F_{11}(\theta)$ and $-F_{12}(\theta)/F_{11}(\theta)$ of terrestrial quartz and clay particles with those of several meteoritic particles. Although these measurements have been performed on single rotating particles, the results are similar to the results for ensembles of randomly oriented particles.

Two characteristic phenomena have been observed for interplanetary dust particles, comets, asteroids, and other celestial bodies [e.g., Lumme, 2000]. First, a sharp maximum in brightness occurs toward the backscattering direction, which is called the opposition effect. Second, the degree of linear polarization for incident unpolarized light, i.e., $-F_{12}(\theta)/F_{11}(\theta)$, negative beyond a scattering angle of about 160°.

We cannot draw definite conclusions about the opposition effect for the mineral particles studied, since our measurements do not reach beyond a scattering angle of 173°. However, most of the experimental phase functions show signs of a modest backscattering maximum (see Figures 5-11). This modest backscattering maximum suggests that the opposition effect for bodies such as the Moon and the zodiacal dust can be explained, at least partly, by the presence of irregular mineral particles.

Regarding the second phenomenon, pertaining to the degree of linear polarization of singly scattered light for incident unpolarized light, many observations are available at phase angles $\alpha < 120°$ ($\alpha = 180° -\theta$) for comets, asteroids, and other celestial bodies [e.g., Chernova et al., 1993; Levasseur-Regourd et al., 1996]. For instance, a number of comets with a maximum degree of linear polarization between 0.10 and 0.28 at $\theta = 85° \pm 10°$ is discussed by Levasseur-Regourd et al. [1996]. These comets have a degree of linear polarization which vanishes at $\theta \sim 160°$ and has a minimum of -0.02 ± 0.01 at around $\theta \sim 170°$. Similar values have been found for, e.g., C-type asteroids [Chernova et al., 1993] and the Martian surface [Dollfus et al., 1984]. Our measurements show a similar behavior, in particular for
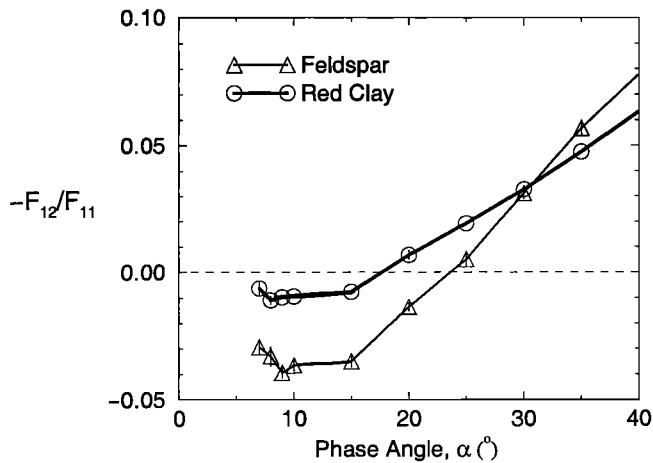
Figure 19. Two examples of the negative branch for the degree of linear polarization for incident unpolarized light, $-F_{12}(\theta)/F_{11}(\theta)$, for the feldspar and red clay samples, both at 441.6 nm. The negative branches measured for the other samples and wavelengths present a similar behavior and are omitted for clarity.

the negative polarization branch at large scattering angles (Figure 19; see also Figures 5-12). The measured $-F_{12}(\theta)/F_{11}(\theta)$ curves at both wavelengths considered change sign between $\theta = 155°$ and $165°$ and have a minimum between -0.01 and -0.04 at nearly $170°$. This suggests that the negative polarization branch at small phase angles exhibited by most solid solar system bodies can be explained, at least in part, by single scattering by small irregular particles.

The wavelength dependence of the maximum in the degree of linear polarization at side-scattering angles is important for the derivation of the characteristics of, for example, cometary particles. For comets the maximal degree of linear polarization usually increases with wavelength [e.g., *Chernova et al.*, 1993], as is the case for most of our aerosol samples, in particular the light-colored ones, i.e., feldspar, quartz, and Pinatubo volcanic ash (Figures 5-11, Figure 12). For the asteroid Toutatis [*Ishiguro et al.*, 1997] a decrease in the degree of linear polarization with wavelength was observed, which is similar to the behavior of the dark brown Lokon volcanic ash sample reported in this paper. This may be due to a higher iron abundance in asteroids as compared to comets.

In conclusion, measurement results such as presented in this paper can potentially reveal valuable information on the physical properties of astronomical dust particles. Measurements on cometary-analog candidates, such as olivine particles, have been reported by *Muñoz et al.* [2000] to aid the interpretation of spaceborne and ground-based observations of comets.

References

Bohren, C. F., and D. R. Huffman, *Absorption and Scattering of Light by Small Particles,* John Wiley, New York, 1983.

Braak, C. J., J. F. de Haan, C. V. M. van der Mee, J. W. Hovenier, and L. D. Travis, Parameterized scattering matrices for small particles in planetary atmospheres, *J. Quant. Spectrosc. Radiat. Transfer, 69,* 585-604, 2001.

Bréon, F. M., J. L. Deuzé, D. Tanré, and M. Herman, Validation of spaceborne estimates of aerosol loading from Sun photometer measurements with emphasis on polarization, *J. Geophys. Res., 102,* 17,187-17,195, 1997.

Chernova, G. P., N. N. Kiselev, and K. Jockers, Polarimetric characteristics of dust particles as observed in 13 comets: Comparison with asteroids, *Icarus, 103,* 144-158, 1993.

Colangeli, L., V. Mennella, C. Di Marino, A. Rotundi, and E. Bussoletti, Simulation of the cometary 10 μm band by means of laboratory results on silicatic grains, *Astron. Astrophys., 293,* 927-934, 1995.

d'Almeida, G. A., P. Koepke, and E. P. Shettle, Atmospheric aerosols, in *Global Climatology and Radiative Characteristics,* A. Deepak, Hampton, Va., 1991.

Deepak, A., (Ed.), *Atmospheric Aerosols: Their Formation, Optical Properties, and Effects,* Spectrum, Hampton, Va., 1982.

Dollfus, A., S. Ebisawa, and E. Bowell, Polarimetric analysis of the Martian dust storms and clouds in 1971, *Astron. Astrophys., 131,* 123-136, 1984.

Draine, B. T., The discrete-dipole approximation and its application to interstellar graphite grains, *Astrophys. J., 333,* 848-872, 1988.

Draine, B. T., The discrete-dipole approximation for light scattering by irregular targets, in *Light Scattering by Nonspherical Particles,* edited by M. I. Mishchenko, J. W. Hovenier, and L. D. Travis, pp. 131-145, Academic, San Diego, 2000.

Dugin, V. P., and S. O. Mirumyants, The light scattering matrices of artificial crystalline clouds, *Izv. Russ. Acad. Sci. Atmos. Oceanic Phys., Engl. Transl. 12,* 988-991, 1976.

Egan, W. G., and T. W. Hilgeman, *Optical Properties of Inhomogeneous Materials: Applications to Geology, Astronomy, Chemistry, and Engineering,* Academic, San Diego, Calif., 1979.

Gerber, H. E., and A. Deepak (Eds.), Aerosols and their climatic effects, in *Proceedings of a Meeting of Experts,*

A. Deepak, Hampton, Va., 1984.

Gerber, H. E., and E. E. Hindman, (Eds.), Light absorption by aerosol particles, in *Technical Proceedings of the First International Workshop on Light Absorption by Aerosol Particles,* Spectrum, Hampton, Va., 1982.

Hansen, J. E., and J. W. Hovenier, Interpretation of the polarization of Venus, *J. Atmos. Sci., 31,* 1137-1160, 1974.

Hansen, J. E., and L. D. Travis, Light scattering in planetary atmospheres, *Space Sci. Rev., 16,* 527-610, 1974.

Herman, M., J. L. Deuzé, C. Devaux, P. Goloub, F. M. Bréon, and D. Tanré, Remote sensing of aerosols over land surfaces including polarization measurements: Application to POLDER measurements, *J. Geophys. Res., 102,* 17,039-17,049, 1997.

Hill, S. C., A. C. Hill, and P. W. Barber, Light scattering by size/shape distributions of soil particles and spheroids, *Appl. Opt., 23,* 1025-1031, 1984.

Holland, A. C., and G. Gagne, The scattering of light by polydisperse systems of irregular particles, *Appl. Opt., 9,* 1113-1121, 1970.

Hovenier, J. W., Measuring scattering matrices of small particles at optical wavelengths, in *Light Scattering by Nonspherical Particles,* edited by M. I. Mishchenko, J. W. Hovenier, and L. D. Travis, pp. 355-365, Academic, San Diego, Calif., 2000.

Hovenier, J. W., and C. V. M. van der Mee, Fundamental relationships relevant to the transfer of polarized light in a scattering atmosphere, *Astron. Astrophys., 128,* 1-16, 1983.

Hovenier, J. W., and C. V. M. van der Mee, Testing scattering matrices, a compendium of recipes, *J. Quant. Spectrosc. Radiat. Transfer, 55,* 649-661, 1996.

Hovenier, J. W., and C. V. M. van der Mee, Basic relationships for matrices describing scattering by small particles, in *Light Scattering by Nonspherical Particles,* edited by M. I. Mishchenko, J. W. Hovenier, and L. D. Travis, pp. 61-85, Academic, San Diego, Calif., 2000.

Hovenier, J. W., H. C. van de Hulst, and C. V. M. van der Mee, Conditions for the elements of the scattering matrix, *Astron. Astrophys., 157,* 301-310, 1986.

Hunt, A. J., and D. R. Huffman, A new polarization-modulation light scattering instrument, *Rev. Sci. Instrum., 44,* 1753-1762, 1973.

Husar, R. B., J. M. Prospero, and L. L. Stowe, Characterization of tropospheric aerosols over the oceans with the NOAA advanced very high resolution radiometer optical thickness operational product, *J. Geophys. Res., 102,* 16,889-16,909, 1997.

Ishiguro, M., H. Nakayama, M. Kogachi, T. Mukai, R. Nakamura, R. Hirata, and A. Okazaki, Maximum visible polarization of 4179 Toutatis in the apparition of 1996, *Publ. Astron. Soc. Jpn., 49,* L31-L34, 1997.

Jäger, C., H. Mutschke, B. Begemann, J. Dorschner, and T. Henning, Steps toward interstellar silicate mineralogy, I, Laboratory results of a silicate glass of mean cosmic composition, *Astron. Astrophys., 292,* 641-655, 1994.

Jaggard, D. L., C. Hill, R. W. Shorthill, D. Stuart, M. Glantz, F. Rosswog, B. Taggard, and S. Hammond, Light scattering from particles of regular and irregular shape, *Atmos. Environ., 15,* 2511-2519, 1981.

Kahn, R., R. West, D. McDonald, B. Rheingans, and M. I. Mishchenko, Sensitivity of multiangle remote sensing observations to aerosol sphericity, *J. Geophys. Res., 102,* 16,871-16,881, 1997.

Kaufman, Y. J., D. Tanré, H. R. Gordon, T. Nakajima, J. Lenoble, R. Frouin, H. Grassl, B. M. Herman, M. D. King, and P. M. Teillet, Passive remote sensing of tropospheric aerosol and atmospheric correction for the aerosol effect, *J. Geophys. Res., 102,* 16,815-16,860, 1997.

Kerr, P. F., *Optical Mineralogy,* McGraw-Hill, New York, 1959.

Kiphardt, M. M. B., Experimental determination of scattering matrices of ice crystals, Dep. of Phys. and Astron., Free University, Amsterdam, Netherlands, 1993.

Klein, C., and C. S. Hurlbut Jr., *Manual of Mineralogy,* John Wiley, New York, 1993.

Konert, M., and J. Vandenberghe, Comparison of laser grain size analysis with pipette and sieve analysis: A solution for the underestimation of the clay fraction, *Sedimentology, 44,* 532-535, 1997.

Kuik, F., Single scattering of light by ensembles of particles with various shapes, Ph.D. thesis, Free University, Amsterdam, Netherlands, 1992.

Kuik, F., P. Stammes, and J. W. Hovenier, Experimental determination of scattering matrices of water droplets and quartz particles, *Appl. Opt., 30,* 4872-4881, 1991.

Levasseur-Regourd, A. C., E. Hadamcik, and J. B. Renard, Evidence for two classes of comets from their polarimetric properties at large phase angles, *Astron. Astrophys., 313,* 327-333, 1996.

Lumme, K. , Scattering properties of interplanetary dust particles, in *Light Scattering by Nonspherical Particles,* edited by M. I. Mishchenko, J. W. Hovenier, and L. D. Travis, pp. 555-583, Academic, San Diego, Calif., 2000.

Lumme, K., and J. Rahola, Light scattering by porous dust particles in the discrete-dipole approximation, *Astrophys. J., 425,* 653-667, 1994.

Macke, A., M. I. Mishchenko, B. E. Carlson, and K. Muinonen, Scattering of light by large nonspherical particles: Ray tracing approximation versus T-matrix method, *Opt. Lett., 20,* 1934-1936, 1995.

Mie, G., Beiträge zur Optik trüber Medien, speziell kolloidaler Metalllösungen, *Ann. Phys., 25,* 377-445, 1908.

Miller, R.L., and I. Tegen, Climate response to soil dust aerosols, *J. Clim., 11,* 3247-3267, 1998.

Mishchenko, M. I., and J. W. Hovenier, Depolarization of light backscattered by randomly oriented nonspherical particles, *Opt. Lett., 20,* 1365-1385, 1995.

Mishchenko, M. I., and L. D. Travis, Satellite retrieval of aerosol properties over the ocean using polarization as well as intensity of reflected sunlight, *J. Geophys. Res., 102,* 16,989-17,013, 1997.

Mishchenko, M. I., and L. D. Travis, Capabilities and limitations of a current FORTRAN implementation of the T-matrix method for randomly oriented, rotationally symmetric scatterers, *J. Quant. Spectrosc. Radiat. Transfer, 60,* 309-324, 1998.

Mishchenko, M. I., A. A. Lacis, B. E. Carlson, and L. D. Travis, Nonsphericity of dust-like tropospheric aerosols: Implications for aerosol remote sensing and climate modeling, *Geophys. Res. Lett., 22,* 1077-1080, 1995.

Mishchenko, M. I., W. B. Rossow, A. Macke, and A. A. Lacis, Sensitivity of cirrus cloud albedo, bidirectional reflectance and optical thickness retrieval accuracy to ice particle shape, *J. Geophys. Res., 101,* 16,973-16,986, 1996a.

Mishchenko, M. I., L. D. Travis, and D. W. Mackowski, T-matrix computations of light scattering by nonspherical particles: A review, *J. Quant. Spectrosc. Radiat. Transfer, 55,* 535-575, 1996b.

Mishchenko, M. I., L. D. Travis, R. A. Kahn, and R. A. West, Modeling phase functions for dustlike tropospheric aerosols using a shape mixture of randomly oriented polydisperse spheroids, *J. Geophys. Res., 102,* 16,531-16,544, 1997.

Mishchenko, M. I., J. W. Hovenier, and L. D. Travis, *Light Scattering by Nonspherical Particles,* Academic, San Diego, Calif., 2000a.

Mishchenko, M. I., W. J. Wiscombe, J. W. Hovenier, and L. D. Travis, Overview of scattering by nonspherical particles, in *Light Scattering by Nonspherical Particles*, edited by M. I. Mishchenko, J. W. Hovenier, and L. D. Travis, pp. 29-60, Academic, San Diego, Calif., 2000b.

Molster, F. J., et al., Low-temperature crystallization of silicate dust in circumstellar disks, *Nature, 40,* 563-565, 1999.

Moroz V. I., Y. M. Gektin, M. K. Naraeva, A. S. Selivanov, and D. V. Titov, Aerosol vertical profile on Mars from the measurements of thermal radiation on the limb, *Planet. Space Sci., 42,* 831-846, 1994.

Moulin, C., F. Guillard, F. Dulac, and C.E. Lambert, Long-term daily monitoring of Saharan dust load over ocean using Meteosat ISCCP-B2 data, 1, Methodology and preliminary results for 1983-1994 in the Mediterranean, *J. Geophys. Res., 102,* 16,947-16,958, 1997.

Muinonen, K., Light scattering by stochastically shaped particles, in *Light Scattering by Nonspherical Particles*, edited by M. I. Mishchenko, J. W. Hovenier, and L. D. Travis, pp. 323-352, Academic, San Diego, Calif., 2000.

Muinonen, K., T. Nousiainen, P. Fast, K. Lumme, and J. I. Peltoniemi, Light scattering by Gaussian random particles: Ray optics approximation, *J. Quant. Spectrosc. Radiat. Transfer, 55,* 577-601, 1996.

Muñoz, O., H. Volten, J. F. de Haan, W. Vassen, and J. W. Hovenier, Experimental determination of scattering matrices of olivine and Allende meteorite particles, *Astron. Astrophys., 360,* 777-788, 2000.

Nakajima, T., M. Tanaka, M. Yamano, M. Shiobara, K. Arao, and Y. Nakanishi, Aerosol optical characteristics in the yellow sand events observed in May, 1982 at Nagasaki, part II, Models, *J. Meteorol. Soc. Jpn., 67,* 279-291, 1989.

Okada, K., A. Kobayashi, Y. Iwasaka, H. Naruse, T. Tanaka, and O Nemoto, Features of individual Asian dust-storm particles collected at Nagoya, Japan, *J. Meteorol. Soc. Jpn., 65,* 515-521, 1987.

Peltoniemi, J. I., K. Lumme, K. Muinonen, and W. M. Irvine, Scattering of light by stochastically rough particles, *Appl. Opt., 28,* 4088-4095, 1989.

Perry, R. J., A. J. Hunt, and D. R. Huffman, Experimental determinations of Mueller scattering matrices for nonspherical particles, *Appl. Opt., 17,* 2700-2710, 1978.

Pollack, J. B., D. Hollenbach, S. Beckwith, D. P. Simonelli, T. Roush, and W. Fong, Composition and radiative properties of grains in molecular clouds and accretion disks, *Astrophys. J., 421,* 615-639, 1994.

Prospero, J. M., R. A. Glaccum, and R. T. Nees, Atmospheric transport of soil dust from Africa to South America, *Nature, 289,* 570-572, 1981.

Reed, S. J. B., *Electron Microprobe Analysis,* Cambridge Univ. Press, New York, 1993.

Rietmeijer, F. J. M., A model for tropical-extratropical transport of volcanic ash in the lower stratosphere, *Geophys. Res. Lett., 20,* 951-954, 1993.

Sasse, C., and J. I. Peltoniemi, Angular scattering measurements and calculations of rough spherically shaped carbon particles, *SPIE Proc., 2541,* 131-139, 1995.

Schütz, L., Long range transport of desert dust with special emphasis on the Sahara, *Ann. N.Y. Acad. Sci., 388,* 515-532, 1980.

Stammes, P., Light scattering properties of aerosols and the radiation inside a planetary atmosphere, Ph.D. thesis, Free University, Amsterdam, Netherlands, 1989.

Tegen, I., and I. Fung, Contribution to the atmospheric mineral aerosol load from land surface modification, *J. Geophys. Res., 100,* 18,707-18,726, 1995.

Tröger, W. E., H. U. Bambauer, F. Taborszky, and H. D. Trochim, *Optische Bestimmung der gesteinsbildenden Minerale Tl, I, Bestimmungstabellen,* Schweizerbart, Stuttgart, Germany, 1971.

van de Hulst, H. C., *Light Scattering by Small Particles,* John Wiley, New York, 1957.

Vermeulen, K., Calculated scattering matrices of randomly oriented spheroids distributed over size and shape: A comparison with laboratory measurements for feldspar, Free University, Amsterdam, Netherlands, 1999.

Warren, J. L., M. E. Zolensky, K. Thomas, A. L. Dodson, L. A. Watts, and S. Wentworth, *Cosmic Dust Catalog,* vol. 15, NASA, 1997.

Weiss-Wrana, K., Optical properties of interplanetary dust: Comparison with light scattering by larger meteoritic and terrestrial grains, *Astron. Astrophys., 126,* 240-250, 1983.

West, R. A., Optical properties of aggregate particles whose outer diameter is comparable to the wavelength, *Appl. Opt., 30,* 5316-5324, 1991.

West, R. A., L. R. Doose, A. M. Eibl, M. G. Tomasko, and M. I. Mishchenko, Laboratory measurements of mineral dust scattering phase function and linear polarization, *J. Geophys. Res., 102,* 16,871-16,881, 1997.

K. Muinonen, Observatory, P.O. Box 14, FIN-00014 University of Helsinki, Finland. (muinonen@cc.helsinki.fi)

T. Nousiainen, Department of Meteorology, P.O. Box

H. Volten, O. Muñoz, E. Rol, J.F. de Haan, W. Vassen, and J.W. Hovenier, Department of Physics and Astronomy, Free University, De Boelelaan 1081, NL-1081 HV Amsterdam, Netherlands. (hester@nat.vu.nl; olga@nat.vu.nl; evert@astro.uva.nl; johan@nat.vu.nl; wim@nat.vu.nl; hovenier@nat.vu.nl)

4, FIN-00014 University of Helsinki, Finland. (tpnousia@cumulus.meteo.helsinki.fi)